Màster en Física Avançada

Especialitat: Física Teòrica

Treball Fi de Màster

PROSPECTS FOR A SEARCH OF INVISIBLE PARTICLES PRODUCTED IN ASSOCIATION WITH SINGLE-TOP QUARKS USING A MULTIVARIATE ANALYSIS IN PROTON-PROTON COLLISIONS AT $\sqrt{s}=14$ TEV WITH THE ATLAS DETECTOR AT THE HL-LHC

Josep Navarro González

Tutor (1): José Enrique García Navarro
Tutor (2): Carlos Escobar Ibáñez

Curs acadèmic 2017/18

Abstract

The expected sensitivity of a search for events with one top quark and missing transverse momentum at the final state is estimated in proton–proton collisions at a centre-of-mass energy of $\sqrt{s} = 14$ TeV with the ATLAS experiment at the HL-LHC. A non-resonant production of an invisible dark matter particle in association with a right-handed top quark is considered, where the W boson from the top quark is required to decay into an electron or a muon and a neutrino. An estimated upper limit of 3.4 TeV based on a BDT-discriminant analysis, at 95% CL, assuming an integrated luminosity of 3.0 ab^{-1}, is set on the non-resonant monotop cross-section.

Contents

1 Introduction and motivation **1**
1.1 The Standard Model 1
1.2 Dark Matter 2
1.3 Motivation of this thesis 4

2 Theoretical Framework **5**
2.1 Monotop production at the LHC 5
2.2 Signal models 6

3 The LHC and the ATLAS Experiment **8**
3.1 CERN and the LHC 8
3.2 The ATLAS detector 9
3.3 Upgraded ATLAS detector at the HL-LHC 11

4 Analysis Strategy **13**
4.1 Signal and background simulation samples 13
4.1.1 Signal samples 13
4.1.2 Background samples 14
4.1.3 Upgrade performance functions 14
4.2 Object definition 15
4.3 Event selection 16
4.3.1 Signal control regions 16
4.3.2 Background control regions 16

5 Training and Application of a Boosted Decision Tree **23**
5.1 Machine Learning in High Energy Physics 23
5.2 A Toolkit for Multivariate Analysis 23
5.3 A Boosted Decision Tree 24
5.3.1 Boosting 25
5.3.2 Overtraining and Pruning 26
5.4 Training of the BDT 27
5.4.1 Performance Evaluation 27
5.4.2 The training variables used 27
5.4.3 The BDT configuration parameters 29
5.5 Application of the BDT 29

6 Sensitivity for discovery or exclusion of monotop signature in the non-resonant model **33**
6.1 Previous published results 33
6.2 Exclusion mass limits 33

7 Conclusions **39**
7.1 Conclusions 39
7.2 Future Work 39

A Evaluation of the available MVA methods **40**

B Significance and S/B for different BDT cuts **41**

Acknowledgements **43**

Chapter 1

Introduction and motivation

The theories and discoveries of thousands of physicists since the 1930s have resulted in a remarkable insight into the fundamental structure of matter: everything in the Universe is found to be made from a few basic building blocks called fundamental particles, governed by four fundamental forces. Our best understanding of how these particles and three of the forces are related to each other is encapsulated in the Standard Model (SM) of particle physics. Finalised in the early 1970s, it has successfully explained almost all experimental results and precisely predicted a wide variety of phenomena. After many experiments, the SM has been established as a well-tested physics theory.

1.1 The Standard Model

The matter around us is made of elementary particles, the building blocks of matter. These particles occur in two basic types called fermions and bosons.

The fermionic family is further classified into two subgroups, the so called leptons and quarks. Each subgroup consists of six particles, which are related in pairs or "generations". The lightest and most stable particles make up the first generation, whereas the heavier and less stable particles belong to the second and third generations. All stable matter in the Universe is made from particles that belong to the first generation; any heavier particles quickly decay to the next most stable level. The three generations of quarks are: the "up quark" and the "down quark" forming the first generation, followed by the "charm quark" and "strange quark", then the "top quark" and "bottom (or beauty) quark". Quarks also come in three different "colours" and they only mix in such ways as to form colourless objects. The six leptons are similarly arranged in three generations – the "electron" and the "electron neutrino", the "muon" and the "muon neutrino", and the "tau" and the "tau neutrino". The electron, the muon and the tau all have an electric charge of ± 1 and a sizeable mass, whereas the neutrinos are electrically neutral and have very little mass.

Regarding the bosons, they are divided in two sectors: the gauge and the scalar sector. In order to introduce the gauge bosons, it is necessary to mention that there are four fundamental forces in the Universe: the strong force, the weak force, the electromagnetic force, and the gravitational force. They work over different ranges and have different strengths. Gravity is the weakest but it has an infinite range. The electromagnetic force also has infinite range but it is much stronger than gravity. The weak and strong forces are effective only over a very short range and dominate only at the level of subatomic particles. Despite its name, the weak force is much stronger than gravity but it is indeed the weakest of the other three. Finally the strong force is the strongest of all four fundamental interactions. At least three of the fundamental forces result from the exchange of force-carrier particles, these are the gauge bosons. Particles of matter transfer discrete amounts of energy by exchanging this kind of bosons. Each fundamental force has its own corresponding gauge boson – the strong force is carried by the "gluon", the electromagnetic force is carried by the "photon", and the "W and Z bosons" are responsible for the weak force. Although not yet found, the "graviton" should be the corresponding force-carrying particle of gravity. The SM includes the electromagnetic, strong and weak forces and all their carrier particles, and explains how these forces act on all of the matter particles. However, the most familiar force in our everyday lives, gravity, is not part of the SM, as fitting gravity comfortably into this framework has proven to be a difficult challenge. The quantum theory used to describe the micro world, and the general theory of relativity used to describe the macro world, are difficult to fit into a single framework. Nobody has managed to make the two mathematically compatible in the context of gauge theories. But luckily for particle physics, when it comes to the minuscule scale of particles, the effect of gravity is so weak as to be negligible. Only when matter is in bulk, at the scale of the human body or of the planets for example, does the effect of gravity dominate. So the SM still works well despite its reluctant exclusion of one of the fundamental forces.

The scalar sector only includes a single scalar boson, which was the last elementary particle which was discovered, on July, 4th 2012 by the ATLAS and CMS experiments at CERN's Large Hadron Collider (LHC) [1] [2]. All measurements point to that the discovered boson is the SM Higgs boson, but it will take further work to determine it unmistakeably. but it will take further work to determine whether or not it is the Higgs boson[1] predicted by the SM. Other types of Higgs-like bosons are predicted by other theories that go beyond the SM, helping the scientific community to better understand the nature of dark matter (DM). A summary of the complete set of elementary particles described above is shown in Figure 1.1.

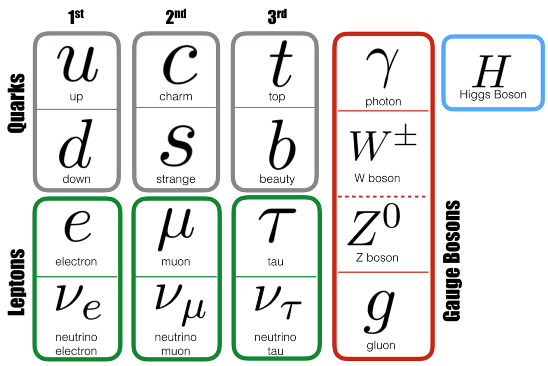

FIGURE 1.1: The SM of elementary particles (schematic depiction), with the three generations of matter, gauge bosons in the fourth column, and the Higgs boson in the fifth.

Even though the SM is currently the best description of the subatomic world, it does not explain the full picture. Apart from the fact that the theory incorporates only three out of the four fundamental forces, there are also important questions that it does not answer, such as "What is dark matter?" (discussed in the next section), "What happened to the antimatter after the Big Bang?", "How do neutrinos get mass?" or "Why are there three generations of quarks and leptons with such a different mass scale?".

1.2 Dark Matter

Galaxies in our Universe seem to behave in an impossible way. As it is was observed by Corbelli and Salucci [5] (see Figure 1.2), they are rotating at such speed that the gravity generated by their observable matter could not possibly hold them together; they should have torn themselves apart long ago. The same is true of galaxies in clusters, which leads scientists to believe that something that cannot be seen is at work. They believe that something that has yet to be detected directly is giving these galaxies extra mass, generating the extra gravity they need to stay intact. This bizarre and unknown matter is what is commonly known as "dark matter" since it is not visible in the electromagnetic spectrum.

[1]The Higgs boson, as proposed within the SM, is the simplest manifestation of the Brout–Englert–Higgs mechanism [3][4] (contributing to our understanding of the origin of mass of subatomic particles).

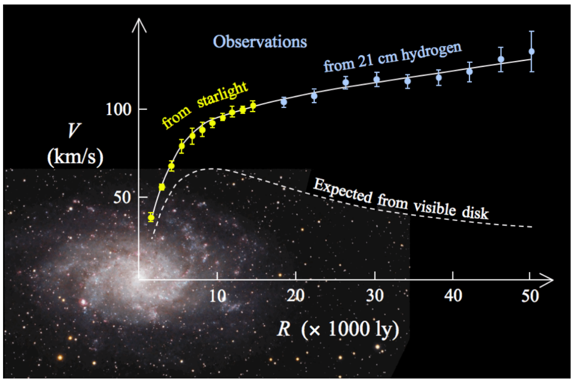

FIGURE 1.2: Rotation curve of spiral galaxy M33 (yellow and blue points with error bars), and a predicted one from distribution of the visible matter (white line). The discrepancy between the two curves can be accounted for by adding a dark matter halo surrounding the galaxy [6].

The study of the cosmic microwave background (CMB), an almost-uniform background of microwaves reaching us from all directions in the sky, is one of the strongest indications of dark matter [7], giving us a precise map of the density of matter in the early Universe. The observed tiny fluctuations, at the level of one part in 100k when the radiation was emitted, grew with time due to gravity, eventually providing the seeds for galaxies and galaxy clusters that are observed today. The shape of the amount of fluctuations, the so-called power spectrum, in the CMB temperature spectrum at different angular scales, is determined by oscillations in the hot gas in the early Universe, while the resonant frequencies of these oscillations and their amplitudes depend on its composition. By analysing the power spectrum, cosmologists were able to determine that our Universe is spatially flat, accelerating, and composed of 5% baryonic matter, 27% cold DM and 68% dark energy.

Unlike normal matter, DM does not interact electromagnetically. This means it does not absorb, reflect or emit light, making it extremely hard to spot. Therefore, in spite of the vast body of evidence, DM is observed merely indirectly: by its gravitational influence on luminous, baryonic matter. So DM seems to outweigh visible matter roughly five to one: as already mentioned, the matter that is known and that makes up all stars and galaxies only accounts for 5% of the content of the Universe. But what is DM exactly? Some, but not all, candidates are outlined in the following lines.

- **Primordial black holes, PBH**: PBHs are those formed before the era of Big-Bang nucleosynthesis. Some cosmological models [8] predict the early creation of a large number of black holes. However, this kind of formation is very constrained from astrophysical observations [9].
- **Axions**: The existence of axions was first postulated to solve the strong CP problem of QCD; they also occur naturally in superstring theories. Although very light, axions would constitute cold DM, since they were produced non-thermally.
- **Sterile neutrinos**: These hypothetical particles are similar to SM neutrinos, but without SM weak interactions, apart from mixing. Stringent cosmological and astrophysical constraints on sterile neutrinos come from the analysis of their cosmological abundance and the study of their decay products [10].
- **WIMPs**: commonly labelled as χ, are particles with masses between 10 GeV and a few TeV, and with cross sections of approximately weak strength. These particles would have been in thermal equilibrium with the hot soup of SM particles after inflation and dropped it out when the rate of the reactions that change SM particles into WIMPs became smaller than the Hubble expansion rate of the Universe (freeze out). After the freeze out, the WIMP density would remain constant and thus one can calculate it. Candidates of WIMPs are neutral lightest superparticles (LSP) in supersymmetric models with exact R-parity [11, 12]. Among the superpartners of ordinary particles, a sneutrino and a neutralino seem the most plausible. Also non-supersymmetric extensions of the SM offer good candidates. Examples

are the lightest T–odd particle in "Little Higgs" models with conserved T–parity [13, 14], or "techni-baryons" in scenarios with an additional, strongly interacting ("technicolor" or similar) gauge group [15].

If one of them was proven to be true, it could help to gain a better understanding of the composition of our Universe and, in particular, how galaxies hold together.

1.3 Motivation of this thesis

Many theories state that the DM particles would be light enough to be produced at the LHC, so even if they would escape through the detectors unnoticed, their existence could be inferred from the amount of energy and momentum "missing" after a collision. However, new physics beyond the SM (BSM) has not been found so far. This would imply that new states or predictions BSM may be much more difficult to spot at the LHC that it was previously thought. In fact, very strong bounds have been posed on *easy-catch* models, like the constrained version of the Minimal Supersymmetric Standard Model [16].

Many theorists have therefore recently turned their attention on a more signature-based strategy, focusing on unusual final states which are difficult to detect or have not been considered yet by experimental collaborations. One such final state that has been gaining popularity among phenomenologists and experimentalists is the "monotop" signature: a single top quark produced in association with a large amount of missing energy, corresponding to the associated production of one or several undetected neutral particles, and without any other reconstructed object. These neutral particles can be either stable and/or weakly interacting with ordinary matter (providing an interesting interpretation in terms of DM candidates) or long-lived and decaying outside of the detector. Production of a monotop signature within the SM is GIM (Glashow–Iliopoulos–Maiani) suppressed so its observation would be clear evidence of BSM phenomena. Moreover, processes involving top quarks are sensitive to BSM physics, due to the large mass of this SM particle which is close to the electroweak symmetry-breaking scale [17].

The main aim of this research project is to provide an event selection criterion that could be applied to a future data sample of proton–proton (pp) collisions (which will be produced by the High-Luminosity LHC at centre of mass energies of 14 TeV and collected by an upgraded ATLAS detector, assuming an integrated luminosity of 3.0 ab^{-1}) in order to optimise the search of the monotop signature. This is conducted via the use of a multivariate analysis (MVA) technique, namely a Boosted Decision Tree (BDT), and Monte Carlo (MC) simulated event signal and background samples (detailed in Chapter 4). The BDT-based method will provide a single discriminant that can be adjusted to optimise theoretical and experimental systematic uncertainties. The new selection should supersede the cut-based method, maximising the ratio of signal to background, S/B, and the statistical significance, $\frac{S}{\sqrt{S+B}}$. Having a sample enhanced in signal events will subsequently allow for a more restrictive bound on the DM candidate (setting new exclusion mass limits).

This work is organised as follows. In chapter 2 the relevant theoretical framework is reviewed. In chapter 3 an overview of the LHC and ATLAS detector and their future upgrades is provided. Chapter 4 provides a description of the simulated samples and analysis tools used in this work. Chapters 5 and 6 contain the main experimental work conducted, of which, 5 details the training and application of a BDT and 6 details the main results on the expected exclusion mass limits once the BDT is applied to our sample. Finally, the conclusions and future work are presented in chapter 7.

Chapter 2

Theoretical Framework

2.1 Monotop production at the LHC

Many BSM theories predict enhanced production of events with large missing energy in association with a single reconstructed object. Such events have been searched for at the LHC, when the single object is either a photon [18, 19], a jet [20, 21, 22, 23], a Higgs boson [24, 25, 26], or a W or Z boson [27, 21, 28]. This work presents a search for singly produced top quarks in association with significant missing energy, corresponding to the associated production of one or several undetected neutral particles, and without any other reconstructed object. As explained above, new phenomena or BSM physics can be evidenced if this final state is observed.

No such process is possible in the SM at tree level. For example, the direct production of a top quark and a Z boson decaying into a pair of neutrinos, without any additional quark, is suppressed by the Glashow–Iliopoulos–Maiani mechanism (see Figure 2.1). Production of such signatures can only be possible at next-to-leading order (NLO)[29].

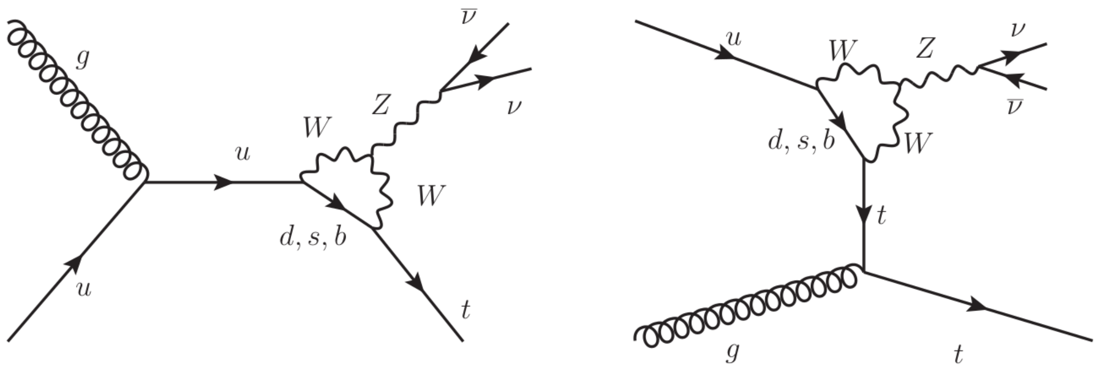

FIGURE 2.1: Feynman diagrams corresponding to the t Z production in the Standard Model (t- and s- channels).

Although it is not easy to obtain this kind of events in realistic and complete models of new physics, two main production mechanisms can lead to a monotop state, arising either from the resonant production of a coloured bosonic state which further decays into a top quark plus an invisible neutral fermion; or via the production of a single top quark in association with an invisible boson that has flavour-changing couplings to top and light-flavour quarks. Examples of the first class of models include R-parity violating supersymmetry, where the produced resonance is a top squark decaying into a top plus a long-lived neutralino [30, 31, 32, 33]. The second class of models has been described in scenarios of DM from a hidden sector that couples to the SM via flavour-violating couplings of a bosonic mediator [34, 35, 36, 37]. In general, monotop signatures can be however generated by other processes involving, for instance, the t-channel exchange of a new particle, different spin assignments for the new states or higher-spin tensors. Motivated by the set-ups currently under study experimentally, this work is limited to the case of a spin-0 or spin-1 state that can be either exchanged in the s-channel (named "resonant" in the following) or produced in association with a top quark via flavour-changing interactions (named "non-resonant").

All such models can be described in terms of a simple Lagrangian, which contains all the possible couplings giving rise to a monotop signal. A very general analysis of this framework can be found in Ref. [38], the limiting case of higher-dimensional operators has been discussed in Ref. [39], while monotop production via flavour-changing interactions of quarks with an invisible Z-boson has been detailed in Ref. [40]. Although this simple description has the advantage of being complete, it has the drawback of containing too many free parameters to be efficiently scanned by an experimental search. Furthermore, the included couplings do not respect the symmetries of the SM, as they are intended to describe the model dynamics after the breaking of the electroweak symmetry. In this way, this approach ignores other interactions needed to restore gauge invariance which can give rise to new physics signals in different search channels, the latter possibly implying stronger constraints on the parameters of the model than the monotop search itself [41].

2.2 Signal models

Many theoretical models predicting the production of monotop events in hadron colliders have been proposed. In a first class of theories, a charged resonance is produced by down-type anti-quark fusion and decays into a top quark and a neutral particle, as in SU(5) models, in R-parity violating SUSY or in hylogenesis models. In a second class of theories, the monotop final state is produced through a non-resonant process, as in R-parity-conserving SUSY, or in models where an interaction of a gluon with an up-type quark allows production of a set of invisible particles via a *u*-*t* or *c*-*t* coupling.

Because of the variety of these theories, effective models are used for the search optimisation reported in this work. Furthermore, as minimal extensions of the SM, the effective model tested in this analysis is required to respect the electroweak gauge structure. The possibilities for monotop production in *pp* collisions are:

- Resonant production of a +2/3 charged spin-0 boson, ϕ, decaying into a right-handed top quark and a neutral, colour singlet, spin-1/2 fermion, χ;
- Non-resonant production of a neutral, colour singlet, spin-1 boson, V, in association with a right-handed top quark. The neutral boson decays to a $\chi\bar{\chi}$ pair.

The Feynman diagrams for monotop production in the resonant and non-resonant models are shown in Fig. 2.2. Each of these effective models corresponds to one of the two classes of BSM theories detailed above. The interaction Lagrangians of the resonant and non-resonants models are given in Eqs. 2.1 and 2.2, respectively.

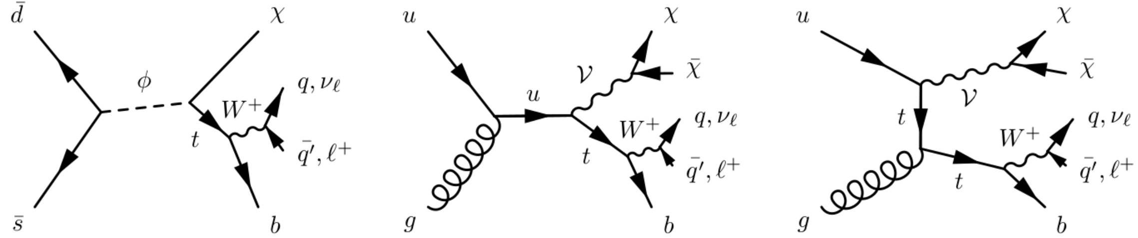

FIGURE 2.2: Monotop production in the context of an effective dark matter model: the leading order Feynman diagrams for the resonant and non-resonant (t- and s- channels) cases are shown.

$$\mathcal{L}_{res} = \epsilon^{\alpha\beta\gamma}\varphi_\alpha \bar{d}^{i,c}_{\beta,R}(a^q_{res})_{ij} d^i_{\gamma,R} + \varphi \bar{u}^k_R (a^{1/2}_{res})_k \chi + h.c. \tag{2.1}$$

$$\mathcal{L}_{non-res} = a_{ij} V_\mu \bar{u}^i_R \gamma^\mu u^j_R + g_\chi V_\mu \bar{\chi}\gamma^\mu \chi + h.c. \tag{2.2}$$

The fields φ, χ, and V_μ correspond ϕ, χ, and V exotic particles, respectively, the field $\bar{u}(\bar{d})$ represents an up-type (down-type) quark, $(a^q_{res})_{ij}$, $(a^{1/2}_{res})_k$, and a_{ij} are the coupling matrices in the quark flavour space, the indices i, j, k, represent the quark generation number, and $\epsilon^{\alpha\beta\gamma}$ is the fully antisymmetric tensor, the indices α, β, γ being the colour indices. The superscript c denotes the charge conjugation. The number of free parameters is reduced by assuming $(a^q_{res})_{12} = (a^q_{res})_{21} = (a^{1/2}_{res})_3 \equiv a_{res}$ for the resonant model and $a_{13} = a_{31} \equiv a$ for the non-resonant model, all other elements of these coupling matrices being equal to 0. For each model, the coupling parameter a_{res} or a and the masses of the exotic particles are independent. In the non-resonant case, the massive invisible vector boson V, also referred in this analysis as v_{met}, is coupled to a DM particle (represented by a Dirac fermion χ) whose strength can be controlled through a parameter g_χ.

The work presented here deals with the non-resonant channel, looking for limits on exclusion for DM for various mediator masses. Moreover, only the topologies where the W boson from the top quark decays into an electron or a muon and a neutrino are considered. Due to the proton composition, the charge of the W boson will usually be positive, and this is considered when defining the different selection regions (Section 4.3).

Chapter 3

The LHC and the ATLAS Experiment

3.1 CERN and the LHC

Established in 1954, the European Organisation for Nuclear Research, CERN, is the research organisation that now hosts the largest laboratory and experiments in particle physics in the World. Situated in Geneva and stretching across the French–Swiss border, CERN is an international collaboration of particle physics, with 22 member states and over 10,000 scientists [42]. At CERN, physicists seek to probe at the fundamental structure of the Universe by investigating the interactions between subatomic particles. This is done through use of large purpose-built particle accelerators and detectors, which generate millions of gigabytes of data to be analysed every year [42]. An overview plan of the particle accelerators found at CERN is illustrated in Figure 3.1.

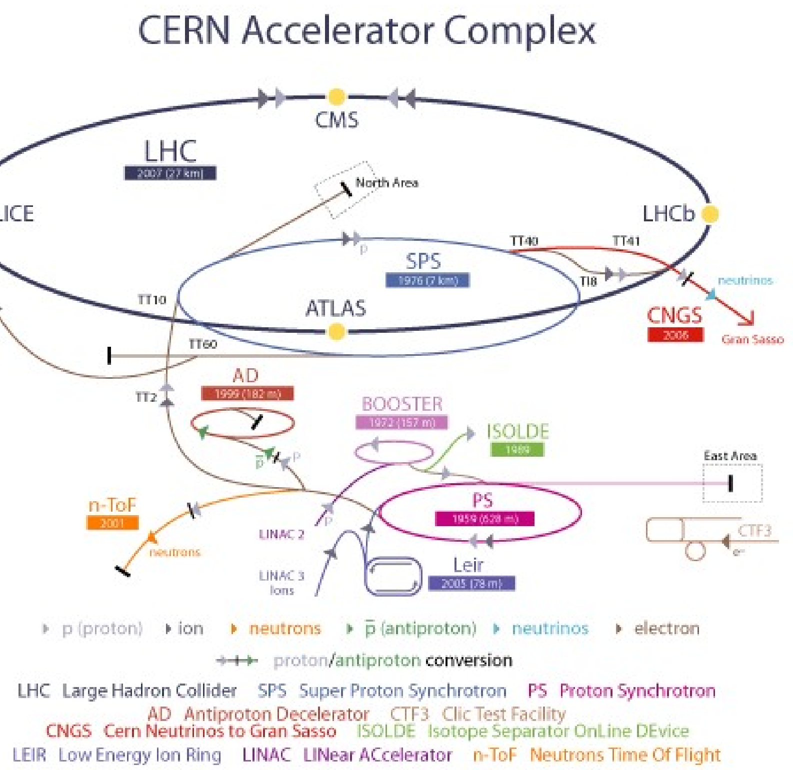

FIGURE 3.1: CERN accelerator complex [43].

The LHC started up in 2008 and is the largest and most powerful of the particle accelerators at CERN and in the world to date [44]. It is an underground circular synchotron with a circumference of 27 km, that accelerates high-energy hadron beams (primarily protons) to near light speed before making them collide at detector sites [44]. The two beams are guided around the accelerator separately in opposite directions through use of strong magnetic fields supplied by superconducting electromagnets located in the ring. Superconducting dipoles curve the trajectory of the protons, quadrupoles focus the beams near the colliding points and the Radio Frecuency cavities accelerate the protons up to the nominal energy and restore the energy losses [45, 46]. The pp collisions at the LHC, involve bunches of up to 10^{11} protons that collide 40 million times per second at various centre-of-mass energies [47].

Along the circumference of the LHC, there are four different interaction points in which different detectors are placed. Figure 3.1 highlights these four detectors; ATLAS, CMS, ALICE and LHCb. ATLAS and CMS are the largest of these experiments - ATLAS being the detector and collaboration within this research is framed.

Accelerator Performance and Parameters

There are several features and parameters essential in the performance of particle accelerators such as the LHC. The energy provided by the colliding beams of a particle accelerator is indicated by the centre-of-mass energy, $\sqrt{s}$ [48]. In general, colliding beams (as opposed to a beam striking a fixed target) are essential to reach the high $\sqrt{s}$ values needed for particle physics [49]. The LHC has operated at different centre-of-mass energies and collision rates, detailed in Table 3.1. Here, the increase in these energies throughout the years is seen as it is progressed from Run 1 (Data collected from 2010-2012) to Run 2 (2015 onwards) [50].

In particle physics, a cross-section, σ, is defined as the probability of an interaction occurring. Processes with low probabilities have small cross sections and are generally of more interest. An important parameter for a particle accelerator operation, linked to cross section, is the luminosity; a quantity that indicates the number of collisions within an accelerator - see equation 3.1. Here it is observed that the number of events per second, N, is proportional to the cross-section of an event, with the instantaneous luminosity, $\mathcal{L}$, acting as the proportionality constant [49].

$$N = \mathcal{L}\sigma \tag{3.1}$$

For two beams colliding, instantaneous luminosity is defined more explicitly as:

$$\mathcal{L} = f \cdot \frac{N_1 N_2 N_b}{4\pi\sigma_x\sigma_y} \cdot F(\theta_c, \sigma_x, \sigma_z) \tag{3.2}$$

where N_1 and N_2 are the number of particles in each beam's bunch (a bunch being a packet of protons), N_b is the number of bunches, f is the bunch revolution frequency, σ_x and σ_y are the RMS transverse beam sizes in horizontal and vertical directions, and F is the factor that accounts for luminosity reduction due to the crossing angle θ_c [51, 49, 52]. Luminosity is hence a function of the beam parameters of an accelerator, such as the LHC, and is subsequently the most important quantity in collider physics besides energy [51]. Additionally, $\mathcal{L}_{int}$, the total integrated luminosity, is the integral of $\mathcal{L}$ with respect to time. It is measured in units of inverse barns b^{-1}, where 1 fb^{-1} corresponds to 10^{12} collisions and 1 barn, b, is $10^{-28}m^2$ [53].

Table 3.1 details the values of such parameters for the LHC at different years. Figure 3.2 illustrates the evolution of ATLAS delivered luminosity and energy over time.

3.2 The ATLAS detector

The ATLAS (A Toroidal LHC ApparatuS) detector is a multi-purpose particle detector with cylindrical geometry and forward-backward symmetry with respect to the interaction point [47]. As illustrated in Figure 3.3, the ATLAS detector is comprised of four main components; the Inner Detector (ID), the Calorimeters, the Muon Spectrometer and the Magnet System. These operate alongside the Trigger and Data Acquisition System and the Computing System [57].

ATLAS uses a right-handed coordinate system with its origin at the nominal interaction point (IP) in the centre of the detector and the z-axis along the beam pipe. The x-axis points from the IP to

Run:		Run I			Run II	
Year:	(Design)	2010	2011	2012	2015	2016
Beam Energy (TeV)	7.0	3.5	3.5	4.0	6.5	6.5
$\sqrt{s}$ (TeV)	14	7	7	8	13	13
Protons/Bunch (10^{11})	1.15	1.0	1.3	1.5	1.1	1.1
Bunch Spacing (ns)	25	150	50	50	25	25
Max Peak $\mathcal{L}$ ($10^{34}cm^{-2}s^{-1}$)	1.0	0.021	0.35	0.77	0.51	1.01
$\mathcal{L}_{int}$ (fb^{-1})	-	0.048	5.5	22.8	4.2	38.5

TABLE 3.1: Different performance parameters of the LHC at different years [54, 55]. Note that the center of mass energy $\sqrt{s}$ is twice that of the beam energy because there are 2 colliding beams.

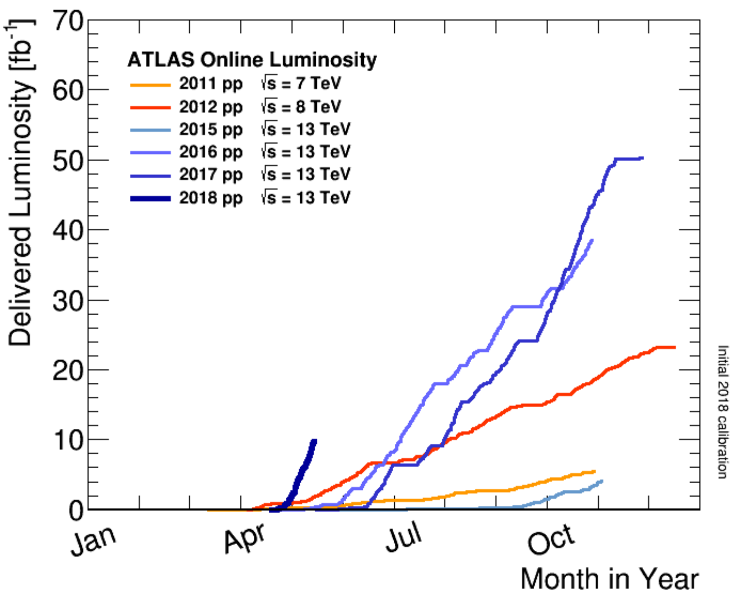

FIGURE 3.2: Delivered Luminosity to ATLAS versus time for 2011-2018 during stable beams and for high energy pp collisions [56]

the centre of the LHC ring, and the y-axis points upward. Cylindrical coordinates (r, ϕ) are used in the transverse plane, ϕ being the azimuthal angle around the z-axis. The pseudorapidity is defined in terms of the polar angle θ as $\eta = -\ln\tan(\theta/2)$. The transverse momentum and energy are defined as $p_T = p \sin\theta$ and $E_T = E \sin\theta$, respectively. The ΔR is the distance defined as $\Delta R = \sqrt{(\Delta\eta)^2 + (\Delta\phi)^2}$.

The ID provides charged particle "tracking" in the pseudorapidity range of $|\eta| < 2.5$. The combination of a high-resolution silicon pixel detector, a silicon microstrip tracker, and a straw-tube transition radiation tracker allow the measurement of particle momenta and vertices and the identification of particle type. For momentum isolation, an axial magnetic field of 2 T surrounds the ID. The energies of these particles are measured by the calorimeters. Liquid Argon (LAr) sampling calorimeters provide electromagnetic energy measurements in the range $|\eta| < 3.2$ whilst hadronic energy measurements in the range $|\eta| < 1.7$ are provided by steel/scintillator-tile calorimeters. The total coverage is extended to $|\eta| = 4.9$ by the presence of LAr calorimeters in the forward region that measure both electromagnetic and hadronic energies [47]. The outermost part of the ATLAS detector, the Muon Spectrometer, surrounds the calorimeter and measures and identifies the muons that pass through the inner regions (ID and Calorimeters) undetected [57].

Due to the large collision rate at the ATLAS design luminosity of $10^{34}cm^{-2}s^{-1}$ (roughly 10^9 collisions per second, corresponding to a data volume of more than $60x10^6$ MB/s [57]) a Trigger System is employed to reduce the number of events selected and stored. Only events with certain distinguishing physical characteristics are chosen, reducing the stored event rate to a more

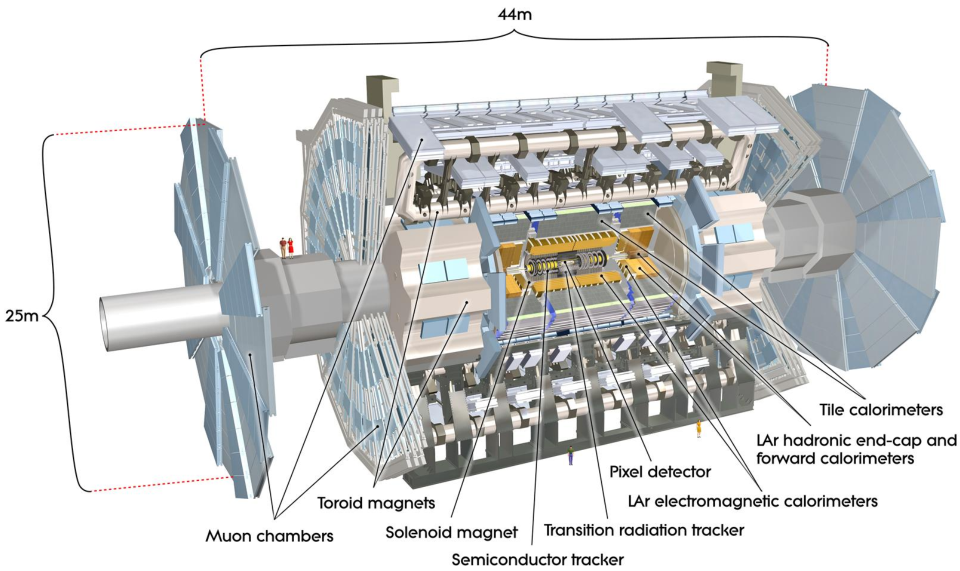

FIGURE 3.3: The ATLAS detector[57]

manageable rate of 1 kHz.

3.3 Upgraded ATLAS detector at the HL-LHC

The HL-LHC is currently expected to begin its operations in the second half of 2026, with a nominal levelled instantaneous luminosity of 7.5×10^{34} cm^{-2} s^{-1}. This will lead to an average number of approximately 200 inelastic pp collisions per bunch-crossing (compared to ~ 25 in 2016 data-taking at 10^{34} cm^{-2} s^{-1}). This programme aims to provide a total integrated luminosity of 3.0 ab^{-1} by 2035 (see Figure 3.4). Upgrades of the ATLAS detector will be necessary to maintain its performance in the higher luminosity environment and to mitigate the impact of radiation damage and detector aging.

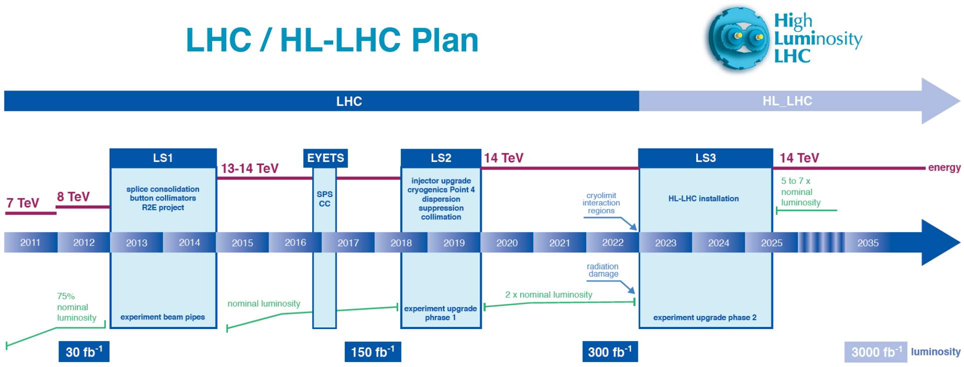

FIGURE 3.4: LHC baseline plan for the next decade and beyond showing the energy of the collisions (upper red line) and luminosity (lower green lines). After LS3, 2023–2025, the machine will be in the High Luminosity configuration (HL-LHC) [58].

The ID will be completely replaced for the HL-LHC, using an all-silicon design (refer to as "ITk") with increased granularity, higher read-out bandwidth and reduced material budget [59, 60]. It will be extended to provide tracking in the region $|\eta| < 4$. The performance of the ITk will be as good, and in most cases better, than the existing ID in an environment with significantly higher pile-up. All of the calorimeters except for the forward calorimeters will maintain their current performance and they will not be replaced, although the readout electronics will be replaced to enable improved triggering [61, 62]. A new high-granularity calorimeters will also be installed in the forward regions to reduce occupancy in the high-pile-up HL-LHC environment. The muon detector will be upgraded [63] in order to: extend coverage for muon identification to $|\eta| < 4$; allow the use of precision tracking for early trigger decisions; reduce the fake trigger rate in the forward region while preserving high efficiency; and increase trigger acceptance by eliminating gaps.

The trigger and data acquisition systems will be improved to preserve high signal acceptance in the high rate, high-occupancy HL-LHC environment [64]. The improvements will include: higher bandwidth readout; using high granularity measurements earlier in the trigger; and using tracking information earlier in the trigger. The final accept rate is planned to be between 5-10 kHz. The b-jet efficiency and light-flavour-quark rejection of the projected ATLAS detector at the HL-LHC is expected to be similar to that of the current detector while the c-jet rejection is expected to be about a factor of two lower than that of the current detector.

Chapter 4

Analysis Strategy

4.1 Signal and background simulation samples

This analysis uses samples of events generated at $\sqrt{s} = 14$ TeV for HL-LHC studies (assuming an integrated luminosity of 3.0 ab^{-1}) using MC simulations produced using different event generators interfaced to various parton showering (PS) and hadronisation generators. After the event generation step, trigger and detector effects were added with the dedicated ATLAS software framework, `Athena` [65] (see Section 4.1.3).

All the signal and background processes involving top quarks were simulated assuming a top-quark mass of 172.5 GeV, and the decay of the top quark was assumed to be 100% $t \to Wb$.

4.1.1 Signal samples

For the matrix-element (ME) calculations, samples of signal events generated using the non-resonant motoptop model were produced using MG5_AMC@NLO(v2.3.3) [66] generator at leading-order (LO) using the NNPDF3.0 LO [67] parton distribution function (PDF) set. The PS and hadronisation were handled by the PYTHIA8 (v8.30) event generator [68] with the A14 [69] set of tuned parameters (tune), using the NNPDF2.3 LO PDF set [70]. The `EvtGen` (v1.6.0) program [71] was used for describing the properties of the bottom and charmed hadron decays. All these MC samples were generated for a range of the mediator masses between $m_V = 1.0$ TeVand 5.0 TeV, in steps of 0.5 TeV with DM masses of 1 GeV, for which this search is sensitive. The values of the coupling parameter a was set to 0.5, and g_χ was set to 1.0. As studied in Ref. [72], the kinematic distributions predicted by the model only have a small dependency on the coupling parameters and therefore all samples were generated using this set of parameters. These simulation samples were normalised considering the LO values for the corresponding cross-sections, computed with MG5_AMC@NLO. Their cross-section values are shown in Table 4.1.

$\mathbf{m}_V$ (TeV)	**cross-section (σ)** [pb]
1.0	0.350
1.5	0.0595
2.0	0.0144
2.5	0.0043
3.0	0.00154
3.5	6.30 $\times 10^{-4}$
4.0	2.95 $\times 10^{-4}$
4.5	1.55 $\times 10^{-4}$
5.0	0.904 $\times 10^{-4}$

TABLE 4.1: Samples of simulated monotop (non-resonant model; $W \to \ell\nu$) events used to estimated the signal in this analysis. The cross-section (σ) column includes the inclusive cross-section times the Branching Ratio ($\mathcal{BR}$) of the $W \to \ell\nu$ decay.

4.1.2 Background samples

Samples of simulated events for background processes include the top-quark production (both $t\bar{t}$ and single-top quark), production of W-boson in association with jets (W+jets), and diboson production.

Samples of simulated events for $t\bar{t}$ production and electroweak production of single-top quarks in the t-channel(in the four-flavour scheme), associated tW and s-channel were produced using the NLO POWHEG-BOX generator [73] coupled with the NNPDF3.0 NLO PDF set (using NNPDF3.04f NLO [70] PDF set for the t-channel and CT10 [74] PDF set in the case of the associated tW production). In the $t\bar{t}$ sample, the resummation damping factor [1], h_{damp}, was set to the one and a half times the top-quark mass (i.e. 258.75 GeV). All these simulation samples except the associated tW were interfaced to PYTHIA8 for the PS, fragmentation and the UE simulation, using the A14 tune and the NNPDF2.3 LO PDF set. For the associated tW production sample was interfaced with PYTHIA6, using the CT10 PDF set and the corresponding Perugia2012 tuneable parameters [75]. For all simulation samples involving top quarks the EvtGen program was used to model bottom and charmed hadron decays. These are normalised using their corresponding production cross-sections.

The W-boson production in association with jets are produced using MG5 generator in which MEs up to two partons are calculated at NLO while LO calculations are used for 3 and 4 partons. The NNPDF30 NNLO PDF set is used. The W+jets processes are normalised to the next-to-next-leading-order (NNLO) cross section. The PYTHIA8 generator is used for the PS, fragmentation and the underlying event (UE).

Samples of diboson events (WW, WZ, and ZZ), containing up to three additional partons where at least one of the bosons decays leptonically, were also produced using the Sherpa generator with the NNPDF3.0 NNLO PDF set. The diboson samples are normalised using their corresponding production cross-sections.

Table 4.2 summarises the signal and background samples used in this analysis.

Process	Generator	Tune	PDFs
Monotop	MG5_aMC@NLO+ PYTHIA8	A14	NNPDF23LO
$t\bar{t}$	POWHEG-BOX+ PYTHIA8	A14	NNPDF23LO
$W \to \ell\nu$+jets	MG5+ PYTHIA8	A14	NNPDF23LO
t-channel	POWHEG-BOX+ PYTHIA8 + MadSpin	A14	NNPDF23LO
s-channel	POWHEG-BOX+ PYTHIA8	A14	NNPDF23LO
tW	POWHEG-BOX+ PYTHIA6 + Photos + Tauola	Perugia2012	CT10
Diboson	Sherpa	–	NNPDF3.0 NNLO

TABLE 4.2: List of MC generators and PDFs used for producing the signal and background processes.

4.1.3 Upgrade performance functions

The studies carried out in this analysis rely on a dedicated fast simulation within the Athena framework based on the parametrisation of detector effects for the upgraded ATLAS detector for the HL-LHC. The trigger, reconstruction and identification efficiencies, the energy and transverse momentum resolution of leptons and jets are computed as function of their η and p_{T} using full simulation studies assuming an upgrade ATLAS detector [76], and are tabulated in functions, called performance functions [77], which provide parametrised estimates of the ATLAS performance at the HL-LHC. These smearing functions are applied to truth-level quantities, and also include a dedicated pile-up overlay library to add pile-up jets to a hard-scatter truth event. The smearing functions assume an instantaneous luminosity of 7.5×10^{34} cm^{-2} s^{-1} and the presence

[1] The resummation damping factor, h_{damp}, is one of the parameters controlling the ME/PS matching in Powheg and effectively regulates the high-p_{T} gluon radiation.

of 200 overlapping events in each bunch crossing [78], being the HL-LHC conditions as already mentioned in Section 3.3. Detailed studies of the performance are given in Ref. [79].

The input ntuples of this analysis are a slimmed and skimmed version of the `DAOD.TRUTH1` derivation samples of simulated signal and background events using `AnalyseTop-21.2.35` [80], which implemented the set of performance functions, including smearing functions and efficiency functions, following the recommendations of the ATLAS Upgrade Physics group. Particle-level kinematic distributions were studied at parton level using a routine written within the Rivet toolkit [81] for the signal ME generation. These studies are beyond the scope of this thesis.

4.2 Object definition

This analysis is performed using only MC simulated processes from pp collision from the HL-LHC at $\sqrt{s} = 14$ TeV. The detector response of the upgraded ATLAS (described in Section 3.3) is emulated applying smearing functions to the simulated final-state particles at truth level as discussed in previous section. Thus particle-level definitions are used for electrons, muons, jets and $E_{\mathrm{T}}^{\mathrm{miss}}$, which are the final-state objects used by this analysis. These objects are constructed from stable particles of the CM event record with a lifetime larger than 0.3×10^{-10} s within the observable η range. The criteria to define the particle-level objects is as follows: Electrons and muons, hereafter referred to as leptons (ℓ), that originate from a W boson decay, including those emerging from a subsequent tau decay. The leptons from hadron decays either directly or via a tau decay are rejected[2]. The selected leptons are dressed with photons within a cone of size $\Delta R = 0.1$, which implies that their final four-momenta are the vector sum of the dressing photons and their original lepton four-momenta. In order to simulate the electron/muon track match requirement (i.e. the overlap removal between electrons and muons), events are reject if a matching in ϕ and θ of 0.005 is found between these two particle-level objects. Lepton candidates are rejected if the p_{T} sum of final-state charged particles, within a cone of radius $R = 10$ GeV$/p_{\mathrm{T}}$, exceeds the 6% of their p_{T}. Identification efficiencies [76] are applied to the lepton candidates to select which particles are identified as leptons. These have their energy, p_{T} and η smeared according to the detector resolution.

Neutrinos are treated as detectable particles and are considered in the same way as electrons or muons, i.e. their parents are required not to be a hadron or quark. The $E_{\mathrm{T}}^{\mathrm{miss}}$ is calculated from the vector sum of true final-state particles within the detector acceptance. The contribution due to pile-up is taken into account before applying detector resolution effects. The smearing functions used are described in [82].

Jets are reconstructed using the anti-k_t algorithm [83] with a radius parameter of 0.4 using Fast Jet [84]. All stable final-state particles are used to reconstruct the jets, except the selected leptons, neutrinos and the photons associated with these leptons. This implies that the b-jet energy is close to that of the b-quark before patronisation and fragmentation. Flavour tagging is performed if the jet is within $|\eta| < 2.5$ applying a tagging efficiency, function of the true flavour of the jet, p_{T} and η. These efficiencies are evaluated considering the latest layout of the ITk detector [85] and using the MTV tagging algorithm [86].

Double counting of electron as jets, may arise from electron energy deposition in the calorimeter being clustered by the jet algorithm. To mitigate such effect jets are removed if within $\Delta R = 0.2$ from a selected electron. After this step, electrons within $\Delta R = 0.4$ from a jet are rejected, they are considered as decay product of the hadrons in the jet. For the same similar reasoning, muons that are within $\Delta R = 0.04 + (10\ \mathrm{GeV}/p_T)$ from a jet are also removed. A fraction of the particle-level jets are removed, according to a fake rate [79], and misidentified as electrons. Energy, p_{T} and η of remaining jets are smeared according to the detector resolution. Pile-up jets are rejected using tracking information.

[2]Since certain CM generators do not include W bosons in the CM event record, an implicit W boson matching is employed to achieve general applicability. This implicit requirement excludes leptons from hadron decays, either directly or via a tau decay.

4.3 Event selection

4.3.1 Signal control regions

The experimental signature of the non-resonant monotop events with W boson decaying leptonically is one isolated lepton from the W-boson decay, large $E_{\mathrm{T}}^{\mathrm{miss}}$, and one jet identified as likely to be originated from a b-quark. As an initial requirement, applied on derivation level (TRUTH1), events having at least one electron or muon with $p_{\mathrm{T}} > 25$ GeV and $|\eta| < 2.5$ and at least one jet with $p_{\mathrm{T}} > 25$ GeV and $|\eta| < 2.5$ are considered. Furthermore, at the analysis level, events are required to contain exactly one lepton with $p_{\mathrm{T}} > 30$ GeV, exactly one jet with $p_{\mathrm{T}} > 30$ GeV identified as a b-tagged jet (using the method discussed in Section 4.2), $E_{\mathrm{T}}^{\mathrm{miss}} > 50$ GeV and a transverse mass of the lepton-$E_{\mathrm{T}}^{\mathrm{miss}}$ system [3] , m_{T}^{W}, larger than 50 GeV. Additionally since the considered monotop process favours final states with positive leptons, a charge asymmetry requirement is applied to further separate signal from background events. This basic event selection defines the preselected region (named as "presel" in the figures). Figure 4.1 shows the most important kinematic variables in this region for the electron and muon channels merged together.

In addition to the preselection requirements, further discrimination between the monotop signal events and background events is achieved by applying additional criteria to the m_{T}^{W} and to the azimuthal difference between the lepton momentum and the b-jet momentum directions, $|\Delta\phi(\ell, b)|$. These two variables are chosen since they have the best discriminant power in the cut-based analysis. As seen in Figure 4.1, the presence of signal is enriched in regions with lower $|\Delta\phi(\ell, b)|$ and higher m_{T}^{W}, while the background decreases significantly. The lepton and the b-jet are closer to each other when originated from the decay of a top quark compared to the case of W+jets and diboson background events. Therefore, a selection imposing the rejection of events with $|\Delta\phi(\ell, b)| < 2.0$ is used. The lower threshold value on m_{T}^{W} is increased to 100 GeV. This region is called "Training" region because here the BDT discriminant is trained as described in Section 5. Figure 4.2 shows the most important kinematic variables in this region for the electron and muon channels merged together.

Finally, it is necessary to define the signal region, SR. This region is being optimised in the ongoing analysis at $\sqrt{s} = 13$ TeV but it will be considered in Section 6 in order to get the corresponding exclusion limits. The values of the cuts are even tighter than the ones used for the Training region. The maximum value allowed for $|\Delta\phi(\ell, b)|$ is 1.2 and the lower threshold value on m_{T}^{W} is increased to 260 GeV.

4.3.2 Background control regions

The dominant background in the signal region is the $t\bar{t}$ production. A minor but not negligible contribution comes from W+jets events. In order to control the normalisation of the $t\bar{t}$ and W+jets processes, dedicated regions are defined, referred to as TCR and WCR respectively. These regions are orthogonal but kinematically close to the signal regions, chosen to be enriched in either $t\bar{t}$ or W+jets events. Both control regions are defined after applying the same preselection as to the signal region, but changing the requirements in the $|\Delta\phi(\ell, b)|$ and m_{T}^{W} variables. In the case of the TCR control region, an additional b-jet is required. The selection criteria applied in these control regions are 60 GeV $< m_{\mathrm{T}}^{W} <$ 100 GeV, while no requirements are applied to $|\Delta\phi(\ell, b)|$. All these selection criteria are the same for the electron and muon channels. Figures 4.3 and 4.4 show the most important kinematic variables in the TCR and WCR regions, respectively, for the electron and muon channels merged together. Figure 4.5 shows the expected background composition in the analysis regions Training, TCR and WCR.

Table 4.3 shows a summary of the event selections used to define the signal and control regions. The expected event yields for each region in the electron and muon channel are given in Tables 4.4 and 4.5, respectively.

[3] The transverse mass of the lepton–$E_{\mathrm{T}}^{\mathrm{miss}}$ system is defined as $m_{\mathrm{T}}^{W} = \sqrt{2 p_{\mathrm{T}}(\ell) E_{\mathrm{T}}^{\mathrm{miss}} \left(1 - \cos\Delta\phi(p_{\mathrm{T}}(\ell), \mathrm{E}_{\mathrm{T}}^{\mathrm{miss}})\right)}$ where $p_{\mathrm{T}}(\ell)$ denotes the modulus of the lepton transverse momentum, and $\Delta\phi(\ell, E_{\mathrm{T}}^{\mathrm{miss}})$ is the azimuthal difference between the lepton momentum and the $E_{\mathrm{T}}^{\mathrm{miss}}$ directions.

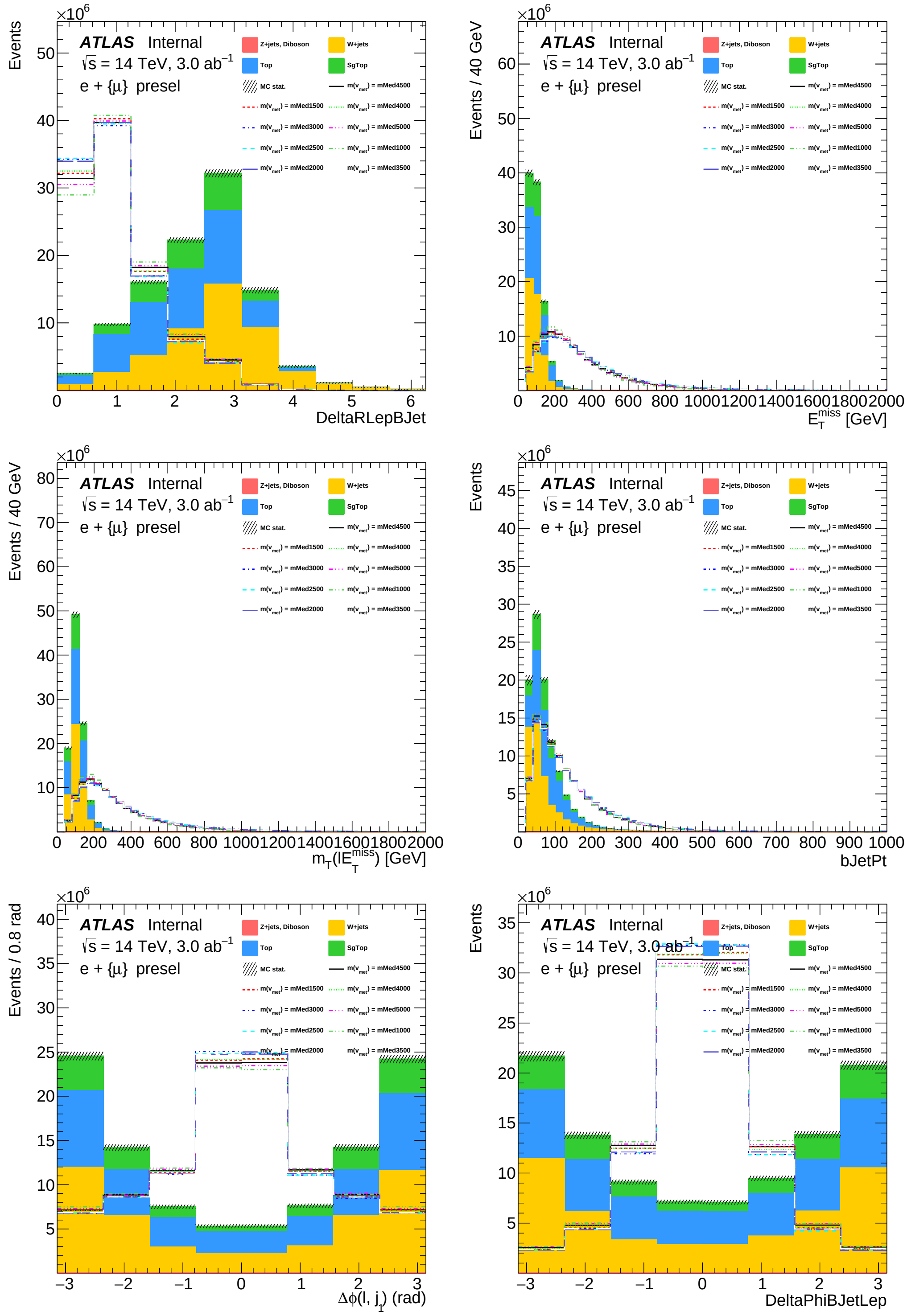

FIGURE 4.1: Distribution of $\Delta R(b,\ell)$, $E_{\mathrm{T}}^{\mathrm{miss}}$, m_{T}^{W}, b-jet p_{T}, $|\Delta\phi(J,\ell)|$ and $|\Delta\phi(\ell,b)|$ in the preselection region for the electron and muon channels merged. Events are required to have exclusively leptons with positive electric charge. The signal non-resonant monotop models with different mediator masses are shown, being normalised to the total expected background yields. The uncertainty band corresponds to the uncertainty due to the size of the simulated event samples.

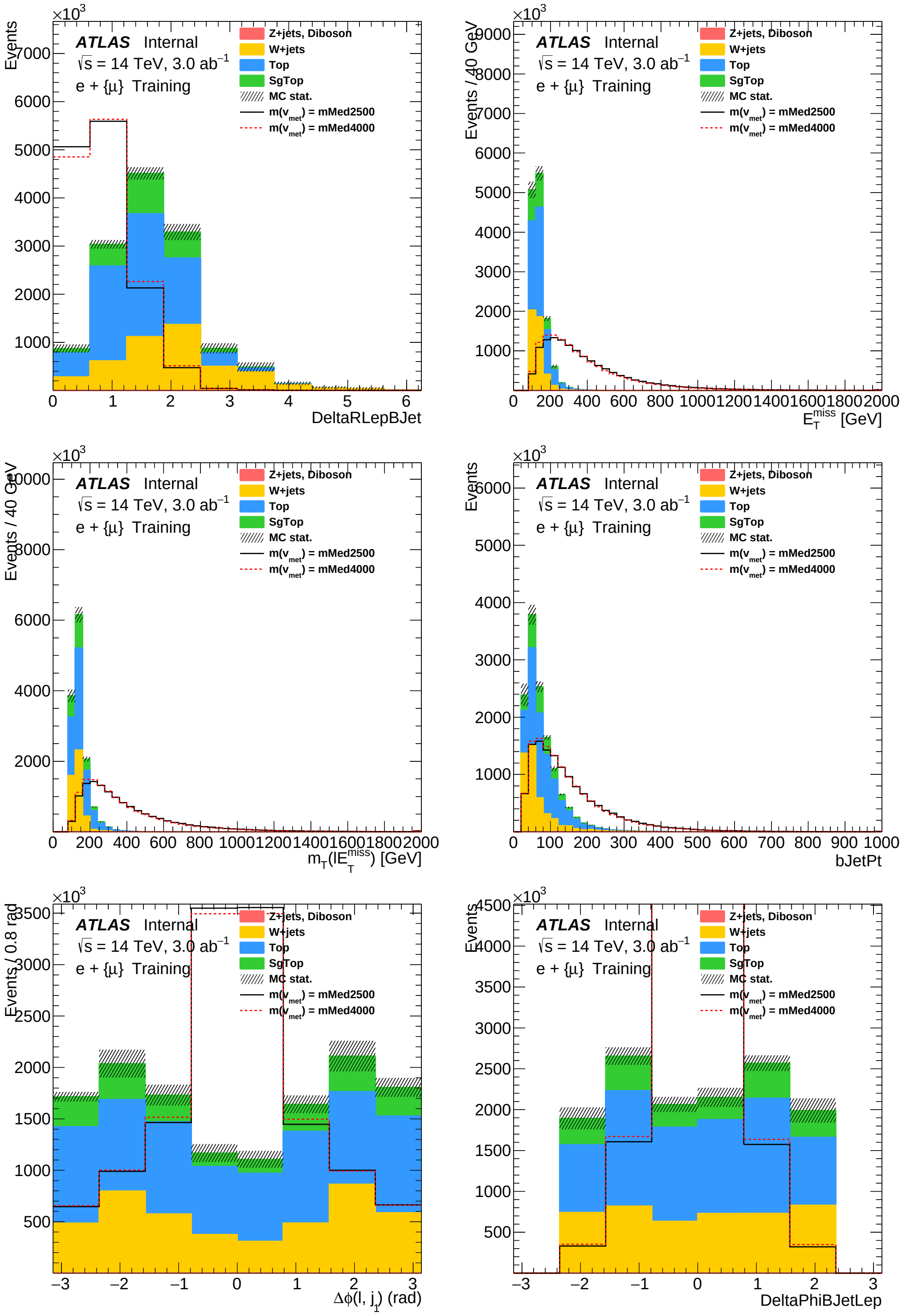

FIGURE 4.2: Distribution of $\Delta R(b,\ell)$, $E_{\mathrm{T}}^{\mathrm{miss}}$, m_{T}^{W}, b-jet p_{T}, $|\Delta\phi(J,\ell)|$ and $|\Delta\phi(\ell,b)|$ in the Training region for the electron and muon channels merged. Events are required to have exclusively leptons with positive electric charge. The signal non-resonant monotop models with different mediator masses are shown, being normalised to the total expected background yields. The uncertainty band corresponds to the uncertainty due to the size of the simulated event samples.

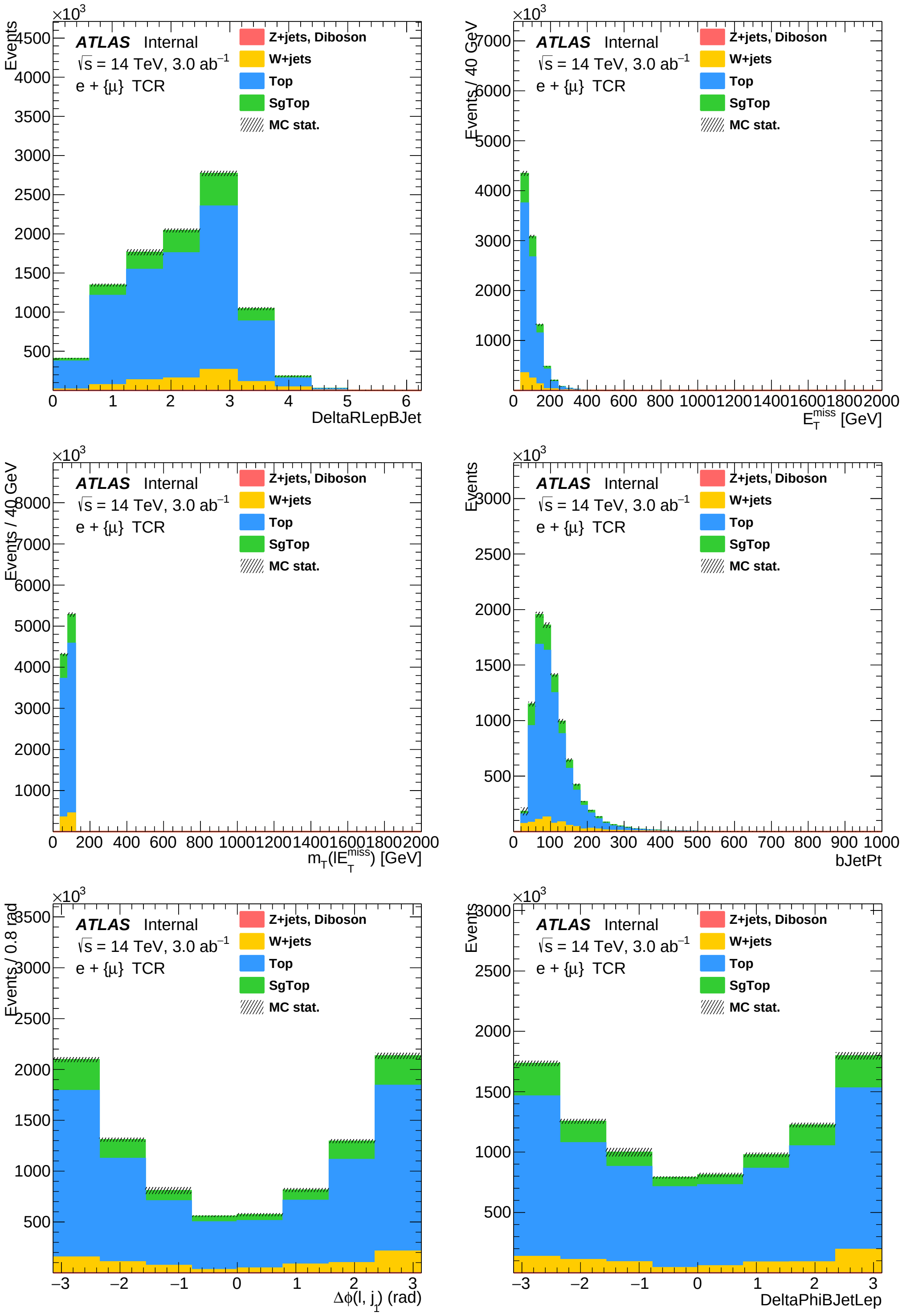

FIGURE 4.3: Distribution of $\Delta R(b, \ell)$, $E_{\mathrm{T}}^{\mathrm{miss}}$, m_{T}^{W}, b-jet p_{T}, $|\Delta\phi(J, \ell)|$ and $|\Delta\phi(\ell, b)|$ in the $t\bar{t}$ control region (TCR) for the electron and muon channels merged. Events are required to have exclusively leptons with positive electric charge. The signal non-resonant monotop models with different mediator masses are not shown here. The uncertainty band corresponds to the uncertainty due to the size of the simulated event samples.

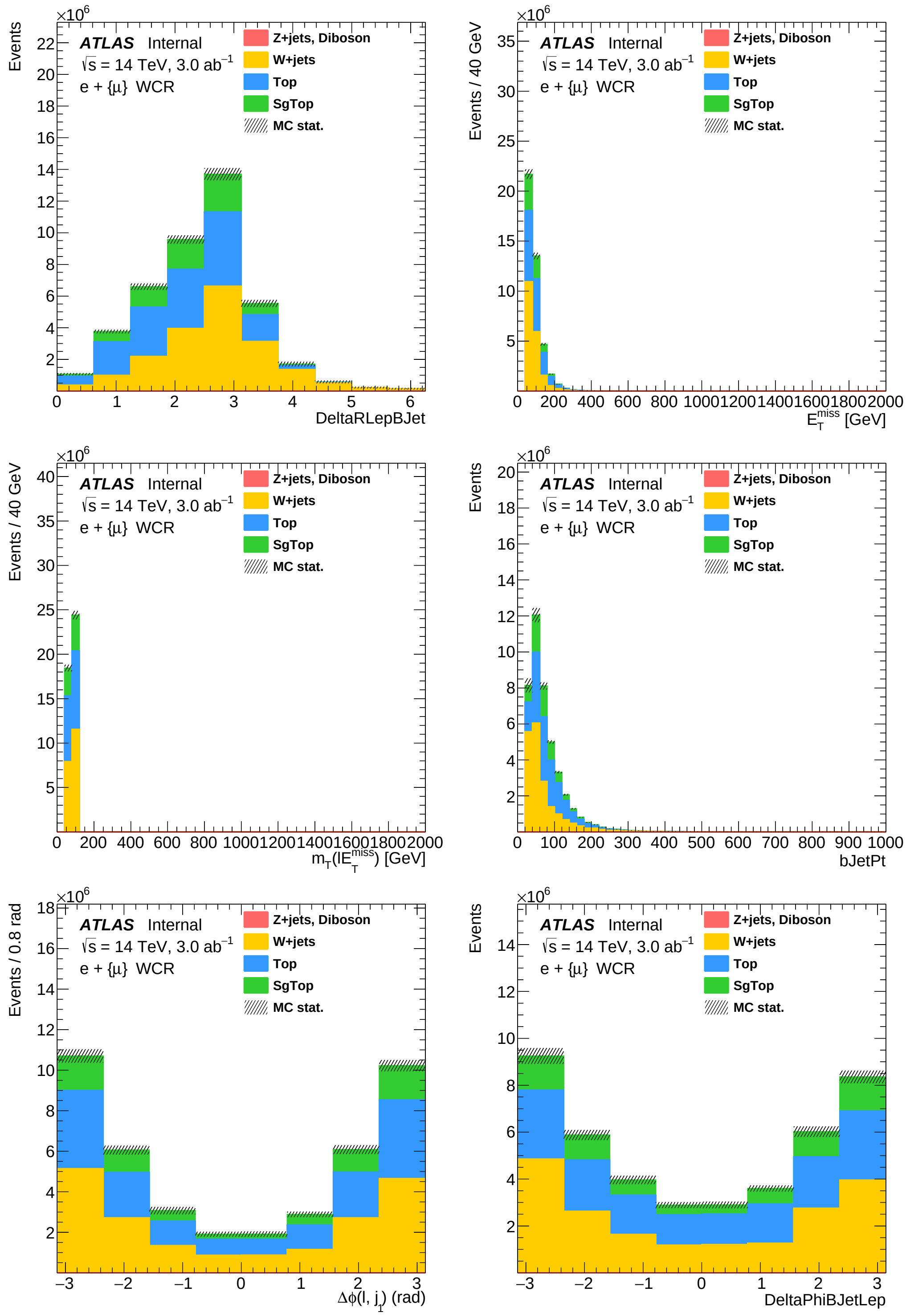

FIGURE 4.4: Distribution of $\Delta R(b,\ell)$, $E_{\mathrm{T}}^{\mathrm{miss}}$, m_{T}^{W}, b-jet p_{T}, $|\Delta\phi(J,\ell)|$ and $|\Delta\phi(\ell,b)|$ in the W+jets control region (WCR) for the electron and muon channels merged. Events are required to have exclusively leptons with positive electric charge. The signal non-resonant monotop models with different mediator masses are not shown here. The uncertainty band corresponds to the uncertainty due to the size of the simulated event samples.

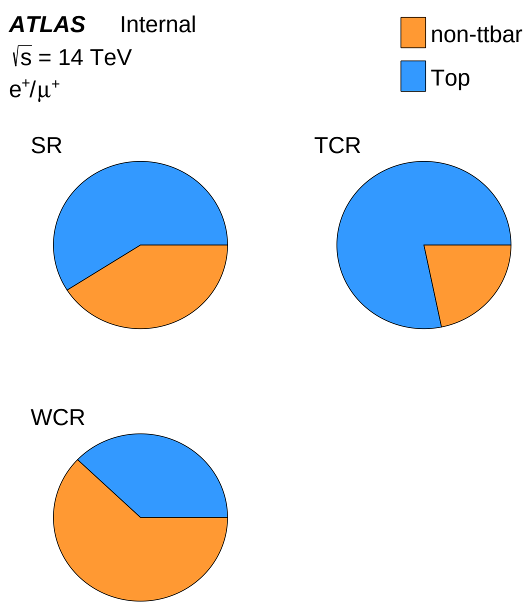

FIGURE 4.5: Relative composition of the backgrounds in the analysis regions in electron and muon channels combined.

Selections	Preselection	Training	SR	TCR	WCR
N(leptons)	1	1	1	1	1
$p_T(\ell)$ [GeV]	> 30	> 30	> 30	> 30	> 30
charge sign	> 0	> 0	> 0	> 0	> 0
p_T (b-jets) [GeV]	> 30	> 30	> 30	> 30	> 30
E_T^{miss} [GeV]	> 50	> 100	> 50	> 50	> 50
N (b-jets)	1	1	1	2	1
m_T^W range [GeV]	> 50	> 100	> 260	[60,100]	[60,100]
$\|\Delta\phi(\ell, b)\|$	–	< 2.0	< 1.2	–	–

TABLE 4.3: Overview of the event selections used to define the signal and control regions.

	Training	WCR	TCR
m_V = 1.0 TeV	85734.99 ± 300.11	6198.06 ± 80.67	183.77 ± 13.89
m_V = 1.5 TeV	15739.90 ± 52.99	982.10 ± 13.24	28.03 ± 2.24
m_V = 2.0 TeV	3946.20 ± 13.06	219.55 ± 3.08	6.57 ± 0.53
m_V = 2.5 TeV	1178.82 ± 3.92	67.23 ± 0.93	2.09 ± 0.16
m_V = 3.0 TeV	407.48 ± 1.37	23.86 ± 0.33	0.71 ± 0.06
m_V = 3.5 TeV	166.88 ± 0.56	9.86 ± 0.14	0.32 ± 0.02
m_V = 4.0 TeV	75.45 ± 0.26	4.75 ± 0.06	0.15 ± 0.01
m_V = 4.5 TeV	38.32 ± 0.13	2.60 ± 0.03	0.08 ± 0.01
m_V = 5.0 TeV	21.80 ± 0.08	1.54 ± 0.02	0.05 ± 0.00
Single-top quark	851611.44 ± 11230.37	2942735.50 ± 19000.51	536628.19 ± 8061.32
$t\bar{t}$	2870870.75 ± 10581.10	6798522.50 ± 16283.63	3173832.75 ± 11118.27
W+jets	1795865.12 ± 194692.12	6731670.00 ± 356782.03	242995.17 ± 33850.14
Diboson	152.10 ± 9.78	113.54 ± 8.28	8.94 ± 2.27

TABLE 4.4: Expected event yields in the electron channel. The uncertainties cover the simulation statistics.

	Training	WCR	TCR
m_V = 1.0 TeV	97411.84 ± 319.95	7691.58 ± 89.87	232.08 ± 15.61
m_V = 1.5 TeV	18084.54 ± 56.82	1265.15 ± 15.03	38.92 ± 2.64
m_V = 2.0 TeV	4477.58 ± 13.91	281.06 ± 3.49	9.86 ± 0.65
m_V = 2.5 TeV	1359.21 ± 4.21	85.63 ± 1.06	2.55 ± 0.18
m_V = 3.0 TeV	481.21 ± 1.49	30.91 ± 0.38	0.98 ± 0.07
m_V = 3.5 TeV	196.32 ± 0.61	12.75 ± 0.16	0.40 ± 0.03
m_V = 4.0 TeV	88.76 ± 0.28	6.27 ± 0.07	0.18 ± 0.01
m_V = 4.5 TeV	44.95 ± 0.14	3.40 ± 0.04	0.10 ± 0.01
m_V = 5.0 TeV	25.44 ± 0.08	2.00 ± 0.02	0.06 ± 0.00
Single-top quark	1207824.62 ± 13294.65	4205243.50 ± 22653.77	746502.50 ± 9387.63
$t\bar{t}$	3910994.00 ± 12348.52	9408212.00 ± 19160.35	4331717.00 ± 12992.84
W+jets	2685945.00 ± 211730.85	12741309.00 ± 499246.23	560312.75 ± 51574.73
Diboson	216.59 ± 11.69	185.06 ± 10.78	11.05 ± 2.64

TABLE 4.5: Expected event yields in the muon channel. The uncertainties cover the simulation statistics.

Chapter 5

Training and Application of a Boosted Decision Tree

The following chapter deals with the selection of a sample enriched in monotop events using BDTs as a MVA. MC simulated event samples at $\sqrt{s} = 14$ TeV for different DM candidates masses have been used.

The uncertainties quoted hereafter are only statistical uncertainties that account for the MC limited statistics and their subsequent appropriate propagations. Systematic uncertainties will not be studied within the time scope of this master thesis, especially since real data is not used, although their estimation will be necessary in further optimisations of the whole analysis chain.

5.1 Machine Learning in High Energy Physics

Machine learning, the field of computer science that gives computers the ability to learn from data without being explicitly programmed [87], is used extensively within research domains such as high energy physics where there exists copious amounts of data and a need for efficient yet innovative analyses. With machine learning techniques, such as neural networks and decision trees, accurate models and predictions can be built without the need for the a priori knowledge or programming of the underlying causal links. The computer instead "learns" solely from the data and its correlations and develops its own conclusion/relationship via automated algorithms [88].

5.2 A Toolkit for Multivariate Analysis

The Toolkit for Multivariate Analysis (TMVA) [89] provides a ROOT-integrated environment for the processing, parallel evaluation and application of multivariate classification and multivariate regression techniques. All multivariate techniques in TMVA belong to the family of "supervised learning" algorithms. They make use of training events, for which the desired output is known, to determine the mapping function that either describes a decision boundary (classification) or an approximation of the underlying functional behaviour defining the target value (regression). TMVA is specifically designed for the needs of HEP applications. Among other MVA techniques, the package includes linear and nonlinear discriminant analysis, Artificial Neural Networks, Support Vector Machine and BDTs.

The TMVA can be run via a simple ROOT script. It allows us to reweight our training and testing MC samples according to its luminosity and cross section. The preparation is done via the class `factory`, i.e.

```
factory → PrepareTrainingAndTestTree(cuts,"options")
```

This includes the precuts and splits our entire sample into test and training samples via the option `SplitMode`. In this analysis, the weights will be imposed to be positive and the set of cuts corresponding to the training region motivated in Chapter 4 will be applied. The splitting is chosen as randomised via the value `Random`. The randomised division is implemented via the random generator `TRandom3`, that is the Mersenne Twister. Moreover, here the samples are split in half for training and the other half for testing. Further, the event weights are renormalised such as the sample is normalised to the number of events (`NumEvents`)

After preparing the sample one can book the MVA method via the function

```
factory → BookMethod(TMVA::Types::kBDT,"BDTG","options")
```

where the last argument is used for further configuration options in the specific method, which will be discussed in the following sections.

Among the several available methods it could be chosen, BDTG (BDT trained with the *Gradient* algorithm) is considered despite its results were compatible with the ones obtained through other MVA techniques such as BDT (BDT trained with the *AdaBoost* algorithm) or Artificial Neural Networks (MLP and MLPBNN). More details on this decision can be found in Appendix A, where the ROC curve (signal efficiency vs. background rejection) is shown for each discussed classifier together with the performance evaluation tables explained below.

5.3 A Boosted Decision Tree

A decision tree is a binary tree structured classifier similar to the one sketched in Figure 5.1. Repeated left/right (yes/no) decisions are taken on one single variable at a time until a stop criterion is fulfilled. The phase space is split this way into many regions that are eventually classified as signal or background, depending on the majority of training events that end up in the final leaf node. The boosting of a decision tree extends this concept from one tree to several trees which form a forest. The trees are derived from the same training ensemble by reweighing events, and are finally combined into a single classifier which is given by a (weighted) average of the individual decision trees. Boosting stabilizes the response of the decision trees with respect to fluctuations in the training sample and it is able to considerably enhance the performance with respect to a single tree [89].

The trees are grown respectively trained in a successive manner, i.e. starting with the root node. The cut value and discrimination variable at each node is chosen, such that it provides the best separation between signal and background. The training stops at a node as soon as the critical lower bound of events (`MinNodeSize`) is reached at that node. The leafs, i.e the final nodes, determine whether the event is signal or background and they are labelled according to their purity $p = \frac{S}{S+B}$. When $p > 0.5$ the event is considered signal and if $p < 0.5$ it is considered background. The quality of separation is defined by the so called impurity function. Different types (`SeparationType`) are the following:

- `Gini Index`: $p \cdot (1 - p)$
- `Cross Entropy`: $-p \cdot ln(p) - (1 - p) \cdot ln(1 - p)$
- `Misclassification error`: $1 - max(1, 1 - p)$
- `Statistical significance`: $\frac{S}{\sqrt{S+B}}$

The training procedure then chooses the variable and cut value, that maximises the increase in the impurity function between an initial node and the sum of the daughter nodes weighted with their corresponding fraction of events. TMVA does this with a granularity set by the parameter `NCuts`. Setting this parameter to the value -1 the TMVA will determine the optimal value of it, i.e the one yielding highest performance.

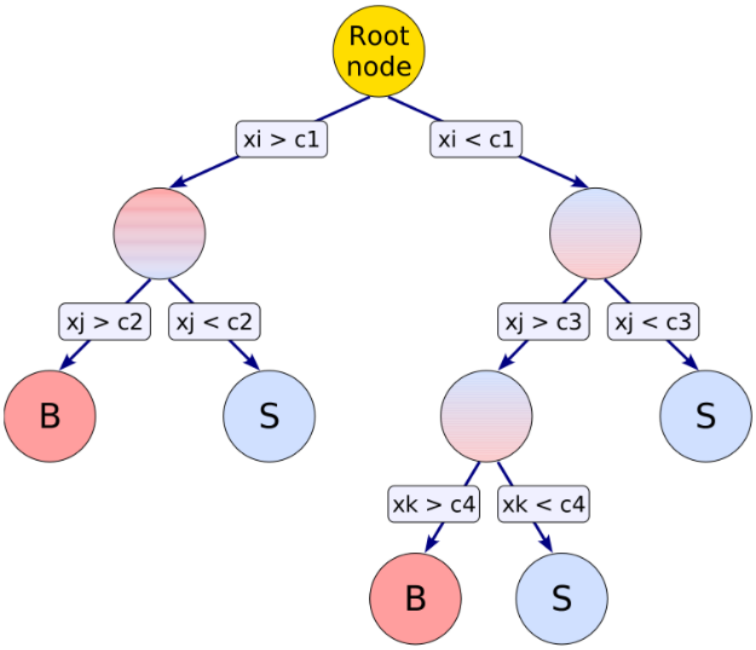

FIGURE 5.1: Schematic view of a decision tree. Starting from the root node, a sequence of binary splits using the discriminating variables x_i is applied to the data. Each split uses the variable that at this node gives the best separation between signal and background when being cut on. The same variable may thus be used at several nodes, while others might not be used at all. The leaf nodes at the bottom end of the tree are labelled "S" for signal and "B" for background depending on the majority of events that end up in the respective nodes [89].

5.3.1 Boosting

Bosting is a way of enhancing the classification performance (and increasing the stability with respect to statistical fluctuations in the training sample) of typically weak MVA methods by sequentially applying an MVA algorithm to reweighed (boosted) versions of the training data and then taking a weighted majority vote of the sequence of MVA algorithms thus produced. It has been introduced to classification techniques in the early '90s and in many cases this simple strategy results in dramatic performance increases.

The most popular boosting algorithm is the so-called *AdaBoost* (adaptive boost). In a classification problem, events that were misclassified during the training of a decision tree are given a higher event weight in the training of the following tree. Starting with the original event weights when training the first decision tree, the subsequent tree is trained using a modified event sample where the weights of previously misclassified events are multiplied by a common boost weight α. This process will go on until a certain `NTrees` are grown, this is then referred to as a forest. The boost weight is derived from the misclassification rate, *err*, of the previous tree,

$$\alpha = \frac{1 - err}{err}$$

The weights of the entire event sample are then renormalised such that the sum of weights remains constant. The result of an individual classifier is defined as $h(x)$, with (x being the tuple of input variables) encoded for signal and background as $h(x) = +1$ and -1, respectively. The boosted event classification $y_{Boost}(x)$ is then given by

$$y_{Boost}(x) = \frac{1}{N_{collection}} \cdot \sum_{i}^{N_{collection}} ln(\alpha_i) \cdot h_i(x) \tag{5.1}$$

where the sum is over all classifiers in the collection. Small (large) values for $y_{Boost}(x)$ indicate a background-like (signal-like) event. Equation 5.1 represents the standard boosting algorithm.

However, this method is based on exponential loss, with the shortcoming that it lacks robustness in presence of outliers or mislabelled data points [89]. The performance of AdaBoost is therefore expected to degrade in noisy settings. The *GradientBoost* algorithm attempts to cure this weakness by allowing for other, potentially more robust, loss functions without giving up on the good immediate performance of AdaBoost. The current TMVA implementation of GradientBooost uses the binomial log-likelihood loss for classification. The boosting algorithm corresponding to this loss function cannot be obtained in a straightforward manner, but it should be remarked that its robustness can be enhanced by reducing the learning rate of the algorithm through the `Shrinkage` parameter which controls the weight of the individual trees.

5.3.2 Overtraining and Pruning

When classifiers are too much adapted to a specific training sample, similar samples can have a completely different response from the trained classifier. In this case one talks of overtraining. Overtraining is problematic as the real data will be classified different from the training sample and the BDT output distribution can not be used to determine the optimal cut value. BDTs are in general sensitive to overtraining. Different techniques called ”pruning” have been developed to deal with this problem in the case of BDTs. The pruning usually refers to the process of cutting down the tree from the leaf-nodes further into the tree removing statistically insignificant nodes. TMVA provides two pruning methods which are `CostComplexity` and `ExpectedError` [90].

The `Cost Complexity` pruning cuts away subtrees, whose gain in classification is not justified by the number of extra nodes required for it. It is defined via the so called cost complexity for a node

$$\rho = \frac{R(node) - R(subtree\,below\,node)}{\#(subtree) - 1}$$

where $R = 1 - max(p, 1 - p)$ is the misclassification error. Nodes with $\rho <$`PruneStrength` are then iteratively cut out of the tree.
Expected Error pruning on the other hand recursively cuts off leaf nodes from the tree, whose combined statistical error

$$err = \sqrt{\frac{p(1-p)}{N}}, \text{ where N is the number of training events in the node}$$

of the leaf nodes is higher than the uncertainty of the parent node. The statistical error might be manipulated by multiplying it with `PruneStrength`.

In the case of `CostComplexity` TMVA provides the option `PruneStrength` $= -1$, which automatically determines the value for `PruneStrength`, that yields the highest performance, by using a subsample of the training sample. This option is not available for `ExpectedError`.

For simple decision trees, it has been found to be beneficial to first grow the tree to its maximum size and then cut back, rather than interrupting the node splitting at an earlier stage. This is because apparently insignificant splits can nevertheless lead to good splits further down the tree. For BDTs however, as the boosting algorithms perform best on weak classifiers, pruning is unnecessary as one should rather drastically limit the tree depth (via the `MaxDepth` parameter) far stronger than any pruning algorithm would do afterwards. Hence, while pruning algorithms are still implemented in TMVA, they are obsolete as they should not be used [89].

5.4 Training of the BDT

5.4.1 Performance Evaluation

The optimal method to be used for a specific analysis strongly depends on the problem at hand and no general recommendations can be given. To ease the choice TMVA computes a number of benchmark quantities that assess the performance of the methods on the independent test sample. In general, the evaluation done in the following sections is based on the Kolmogorov-Smirnov test (K-S test), which evaluates the goodness of consistency between the training/test output distributions. The K-S value is distributed between 0 and 1: the more it is close to 0, the worse is the performance. The test can usually be considered as an overtraining check.
TMVA provides another set of criterion which will be applied when ranking the variables used in the final training configuration [89]:

- The **signal efficiency at three representative background efficiencies** (the efficiency is equal to 1-rejection) obtained from a cut on the classifier output. Similarly, it will be considered the also given integral of the ROC curve (R): the area of the background rejection versus signal efficiency function (the larger the area the better the performance).
- The **separation** $\langle S^2 \rangle$ of a classifier y, defined by the integral

$$\langle S^2 \rangle = \frac{1}{2} \int \frac{(\hat{y}_S(y) - \hat{y}_B(y))^2}{\hat{y}_S(y) + \hat{y}_B(y)} dy$$

  where y_S and y_B are the signal and background probability density functions of y, respectively. The separation is zero for identical signal and background shapes, and it is one for shapes with no overlap.
- The **discrimination significance (D)** (of a classifier, defined by the difference between the classifier means for signal and background divided by the quadratic sum of their root-mean-squares.

The results of the evaluation are printed to standard output. Smooth background rejection/efficiency versus signal efficiency curves (namely ROC curves) are written to the output ROOT file, and can be plotted using custom macros.

5.4.2 The training variables used

In order to make the choice of variables used for the training, the default configuration of the BDTG [1] is considered . The selection method consists in carrying out test trainings where variables will be selected out of the initial complete set. Since discriminating variables (those whose signal distribution differs to the background one) are the ones useful for the BDT training, the variables containing the ϕ information of an object are initially discarded. Furthermore, variables containing the η information are also rejected after a K-S test is performed. A minimum number of variables is then selected in such a way that the optimal training performance is not lost. A full list and description of these variables is given in Table 5.1

A ranking among the final configuration variables is also performed using the set of criterion described in the previous section (Table 5.2). The variables are evaluated according to their change in the ROC-integral (R), separation (L) and discrimination significance (D) with respect to the complete configuration, whose values are 0.948, 0.650 and 1.908 respectively. The more the variable changes these values, the more impact it has on the BDT performance. The closer they are to the complete configuration ones, the less important is the variable (for instance, the smaller the ΔR is, the less relevant is the considered variable).

[1] `NTrees=1000:MinNodeSize=2.5%:BoostType=Grad:Shrinkage=0.10:nCuts=20:MaxDepth=2`

Variable name	Description
E_T^{miss}	Missing transverse momentum
$\Delta\phi(J,\ell)$	$\Delta\phi$ between the leading-jet (J) and the lepton
$\Delta R(b,\ell)$	ΔR between the b-jet and the lepton
Leading-jet p_T	Transverse momentum of the leading jet
$\Delta\phi(b,\ell)$	$\Delta\phi$ between the b-jet and the lepton
b-jet p_T	Transverse momentum of the b-jet
Lepton p_T	Transverse momentum of the lepton
$\Delta R(J,\ell)$	ΔR between the leading jet and the lepton
$\Delta\phi(E_T^{miss},\ell)$	$\Delta\phi$ between E_T^{miss} and the lepton
m_T^W	Transverse mass of lepton and E_T^{miss} system
Leading-jet mass	Mass of the leading jet

TABLE 5.1: List of variables entering the BDT and their definitions. The symbol J indicates the leading jet. The symbol ℓ indicates e and μ.

Excluded variable	**ΔR**	$\Delta\langle S^2\rangle$	**ΔD**
E_T^{miss}	0.006	0.020	0.089
$\Delta\phi(J,\ell)$	0.005	0.013	0.059
$\Delta R(b,\ell)$	0.003	0.009	0.036
Leading-jet p_T	0.002	0.006	0.025
$\Delta\phi(b,\ell)$	0.002	0.006	0.023
b-jet p_T	0.002	0.006	0.022
Lepton p_T	0.002	0.006	0.019
$\Delta R(J,\ell)$	0.002	0.005	0.019
$\Delta\phi(E_T^{miss},\ell)$	0.002	0.005	0.019
m_T^W	0.002	0.005	0.020
Leading-jet mass	0.002	0.005	0.018

TABLE 5.2: Final configuration variables ranking (from best to worst ranked)

Finally, the matrices indicating the correlation among the different studied variables are shown for signal and background distributions in Figure 5.2 for both signal and background samples.

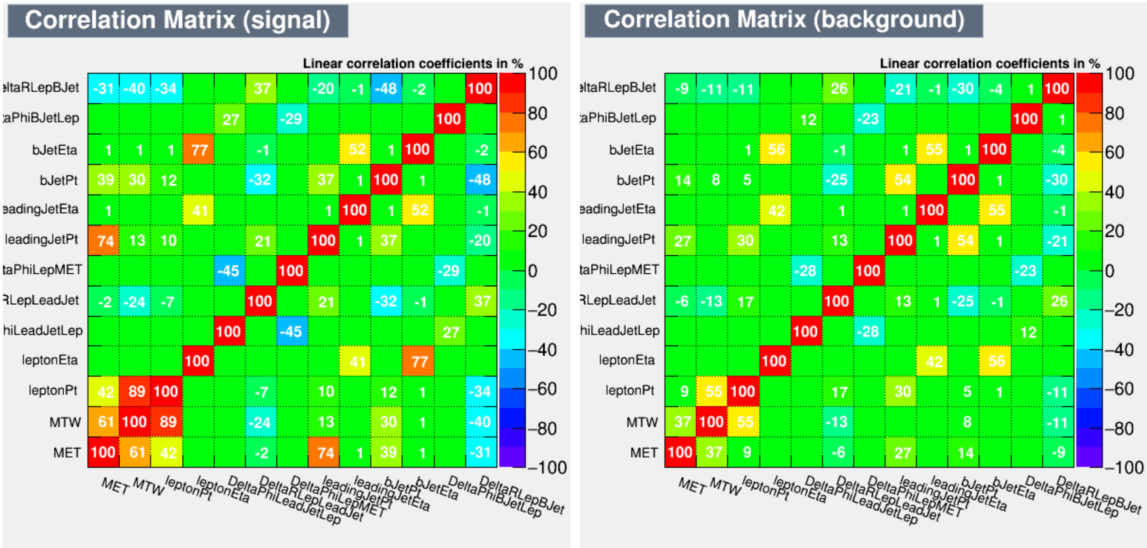

(A) Input variable correlation matrix for signal. (B) Input variable correlation matrix for background.

FIGURE 5.2: Input variable correlation matrices for signal and background samples.

5.4.3 The BDT configuration parameters

Default configurations of the methods should give satisfying performance in average applications. However, paraphrasing the TMVA user's guide, *to solve a concrete problem, all methods require at least some specific tuning to deploy their maximum classification or regression capabilities* [89].

Following the basis of the training variables selection, benefit of the K-S test is get in order to decide which value is optimal for each parameter. In particular, five basic parameters of the BDT (already described in Section 5.3) are studied: the maximum depth of each tree (MaxDepth), the minimum percentage of events at each node (MinNodeSize), the number of cuts each variable receives before it is decided where to cut (nCuts), the number of trees in the "forest" (NTrees) and the parameter which controls the gradient descent of the boost (Shrinkage). Table 5.3 contains the results of the K-S test performed in both signal and background distributions for each value of the parameter considered.

According to these results, a more optimal BDT training can be achieved by changing the Shrinkage parameter from 0.10 to 0.20 and the number of cuts (nCuts) from 20 to 30, since the latter gives a better goodness of signal consistency maintaining a high background K-S test value . The chosen final configuration is then:

```
NTrees=1000:MinNodeSize=2.5%:BoostType=Grad:Shrinkage=0.20:nCuts=30:MaxDepth=2
```

where NTrees, MinNodeSize and MaxDepth keep their default values.

5.5 Application of the BDT

In this section, a set of plots giving more information about the performance of the BDT are first presented. Then, the BDT is applied to our sample in the preselection, training and signal regions. Finally, the S/B and statistical significance are calculated for each cut in the BDT output ($oBDT$).

MaxDepth				
1	**2**	**3**	**5**	**1**
0.007 (0.508)	0.102 (0.672)	0.187 (0.039)	0.016 (0)	0 (0)

MinNodeSize				
0.5%	**1.5%**	**2.5%**	**3.5%**	**5.5%**
0.034 (0.481)	0.047 (0.301)	0.099 (0.44)	0.053 (0.458)	0.041 (0.338)

nCuts				
10	**15**	**20**	**25**	**30**
0.192 (0.427)	0.028 (0.691)	0.129 (0.391)	0.084 (0.228)	0.129 (0.679)

NTrees				
50	**500**	**1000**	**1500**	**2500**
0.017 (0.47)	0.103 (0.428)	0.133 (0.504)	0.145 (0.41)	0.127 (0.157)

Shrinkage				
0.02	**0.05**	**0.10**	**0.15**	**0.20**
0.01 (0.552)	0.029 (0.149)	0.103 (0.442)	0.111 (0.27)	0.127 (0.396)

TABLE 5.3: K-S test results for signal (background) distributions depending on the considered parameter value.

The $oBDT$ distribution is depicted in Figure 5.3. It can be observed an accumulation of background events near -1 and the signal events peak close to +1 for the training sample. Moreover, a good agreement can be observed between the training and test samples.

The ROC-curve is one of the most relevant plots that every cut based analysis usually includes, showing the signal efficiency versus background rejection. A high value of this curve integral (small lose of signal efficiency and background rejection) is desired. The ROC-curve corresponding to the final training is represented in Figure 5.4, yielding to the maximum value achieved for the ROC-curve integral: 0.948.

Figure 5.5 shows the signal and background efficiencies, obtained from cutting on the BDT classifier output, versus the cut value. Also shown are the signal purity and the signal efficiency times signal purity corresponding to 1000 events of signal and 1000 events of background before cutting on $oBDT$. The optimal cuts according to the best significance are printed on standard output.

Once the BDT is trained, it is applied to our complete signal and background samples, i.e a BDT value is added to each event. The distribution of $oBDT$ for the training region is shown in Figure 5.6.

Some orientative plots showing the signal to background ratio (S/B) vs. the statistical significance ($\frac{S}{\sqrt{S+B}}$) for each cut on $oBDT$ are presented in the Appendix B. The granularity of the BDT cut is set to 0.02 and the plots are produced for each region considered in this analysis. As expected, the higher the BDT cut value is, the more the point is moving towards the top-right corner of the plot.

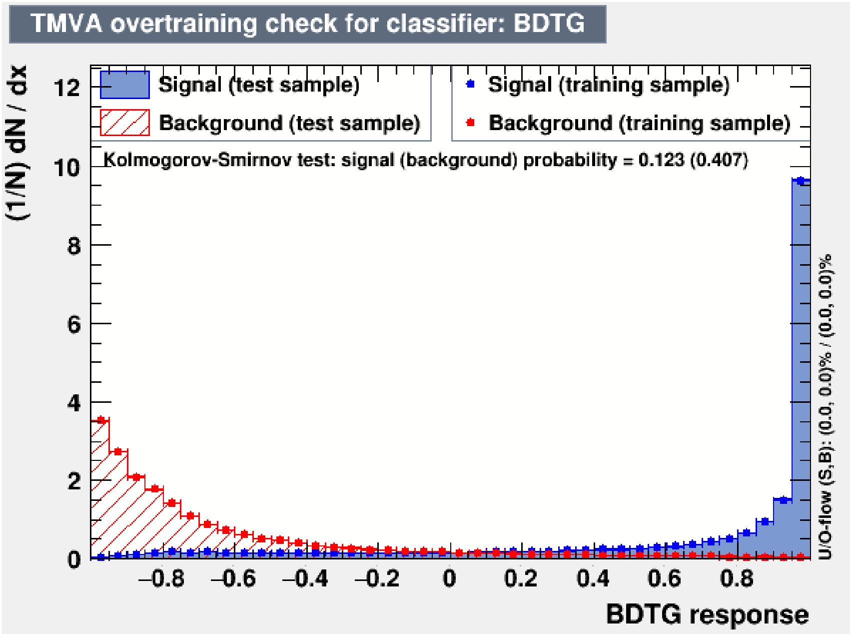

FIGURE 5.3: *oBDT* distribution for the final training configuration and its test, i.e overtraining check.

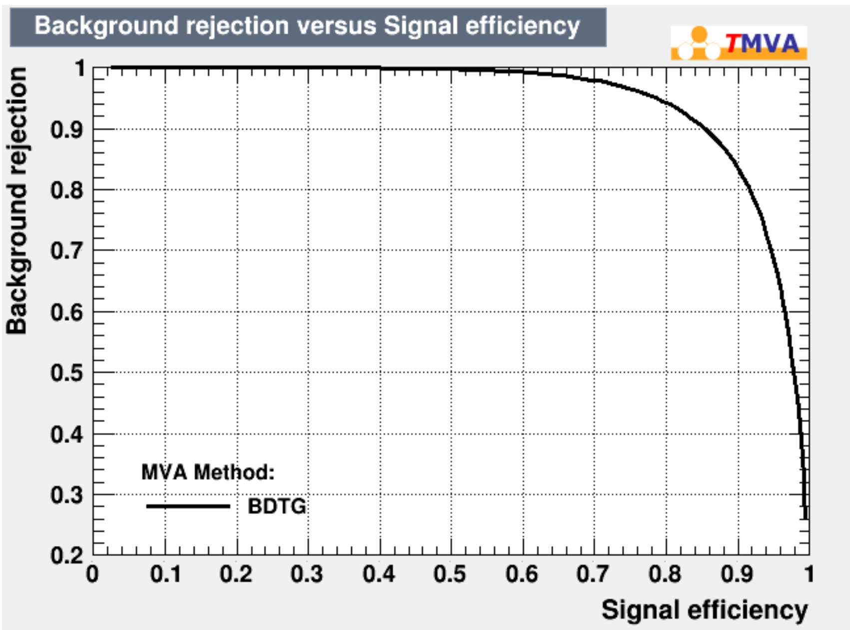

FIGURE 5.4: ROC-curve, i.e. signal efficiency versus background rejection distribution.

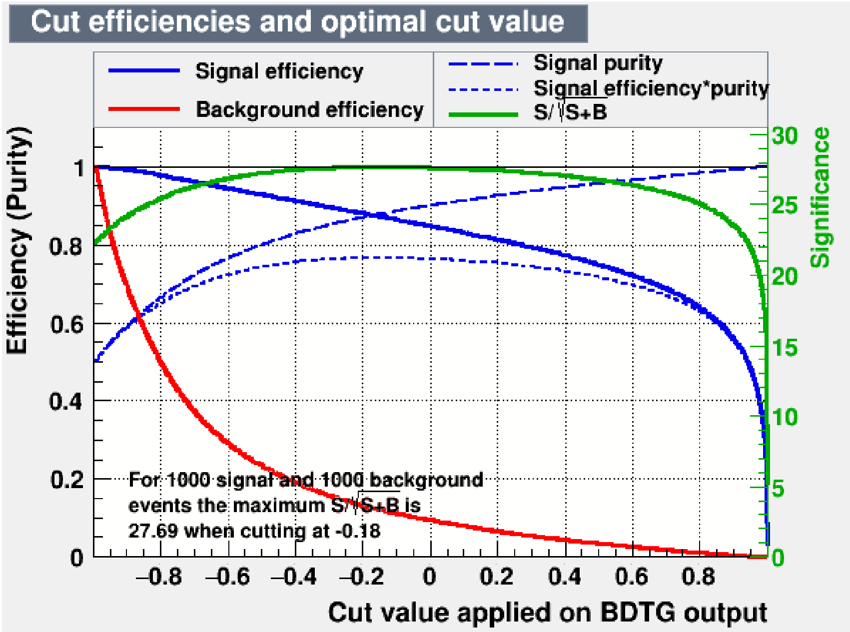

FIGURE 5.5: Classifier cut efficiencies, showing the significance $\frac{S}{\sqrt{S+B}}$, signal and background efficiencies and signal purity as a function of the $oBDT$ cut value.

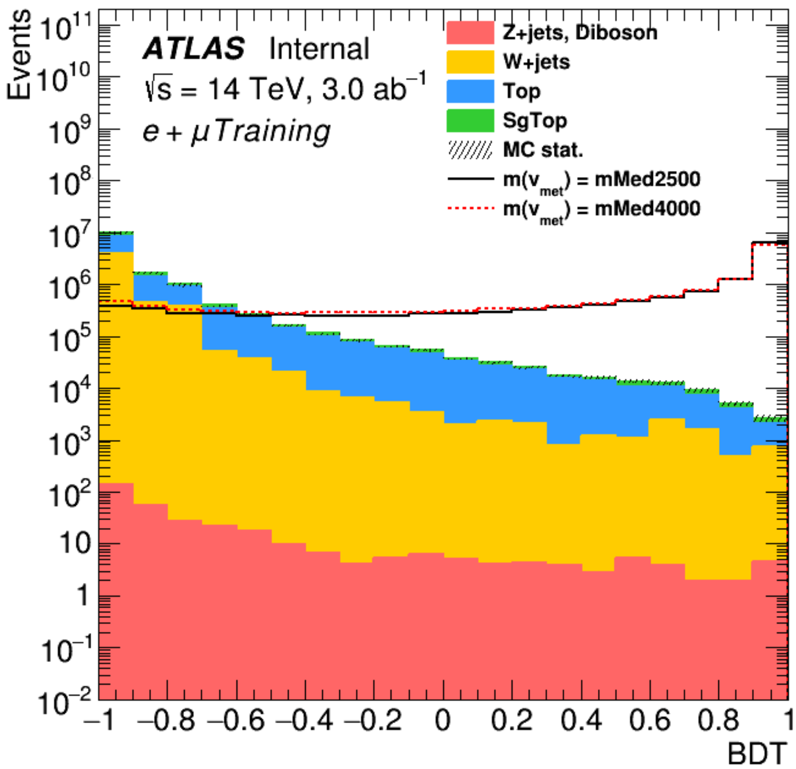

FIGURE 5.6: $oBDT$ distribution for the training region.

Chapter 6

Sensitivity for discovery or exclusion of monotop signature in the non-resonant model

This chapter deals with a study of the exclusion limits in the mass of the DM candidate in order to evaluate the impact of a selection based on a BDT. The BDT based optimisation from chapter 5 has been applied to the MC samples. As mentioned, a new variable in the analysis is considered: the BDT-discriminant, $oBDT$. An investigation into the dependence of this variable on the exclusion limit when cutting at different values is performed for different regions.

6.1 Previous published results

Monotop events were searched for at $\sqrt{s} = 8$ TeV pp collision data collected in 2012 by the ATLAS experiment at the LHC corresponding to an integrated luminosity of 20.3 fb^{-1} [91]. The two classes of signal models were studied, producing right-handed top quarks together with exotic neutral particles giving rise to missing energy. The semileptonic decay mode of the top quark was exploited: events with one isolated electron or muon and one b-tagged jet were selected. No significant deviation from the SM predictions was observed. Upper limits on the signal cross-sections and on the corresponding effective couplings were set at 95% confidence level (CL) using the CLs method. In the case of non-resonant production, effective coupling strengths above a = 0.1, 0.2, and 0.3 were excluded for a mass of the invisible spin-1 state up to 432 GeV, 657 GeV, and 796 GeV, respectively. The observed 95% CL limits were compatible with the expectations. Results obtained for the observed and expected limits on the cross-section times branching ratio (X) for the non-resonant model are interesting for this work. These limits are plotted as a function of the DM candidate mass, $m(v_{met})$, and are shown in Figure 6.1.

Similar searches for such topologies were also done by the CDF Collaboration in proton-antiproton ($p\bar{p}$) collisions at $\sqrt{s}$ = 1.96 TeV at the Tevatron, using 7.7 fb^{-1} [92] and by CMS collaboration using 19.7 (36) fb^{-1} of pp collision data at $\sqrt{s}$ = 8 (13) TeV [93] ([94]) at the LHC. In the CMS search, mediator masses between 0.20 and 1.75 TeV were excluded at 95% CL, given a sufficiently small DM mass. Limits were also calculated as a function of the couplings between quarks and the mediator, fixing m_χ = 1 GeV. The corresponding exclusion in the planes spanned by the coupling and m_V is shown in Figure 6.2.

6.2 Exclusion mass limits

In this section, the main results of this work are presented. First, exclusion mass limits on the invisible DM candidate are calculated for each studied region. Then, using the BDT output as the most discriminant variable, cuts from 0 to 1 are applied to its distribution in the three regions

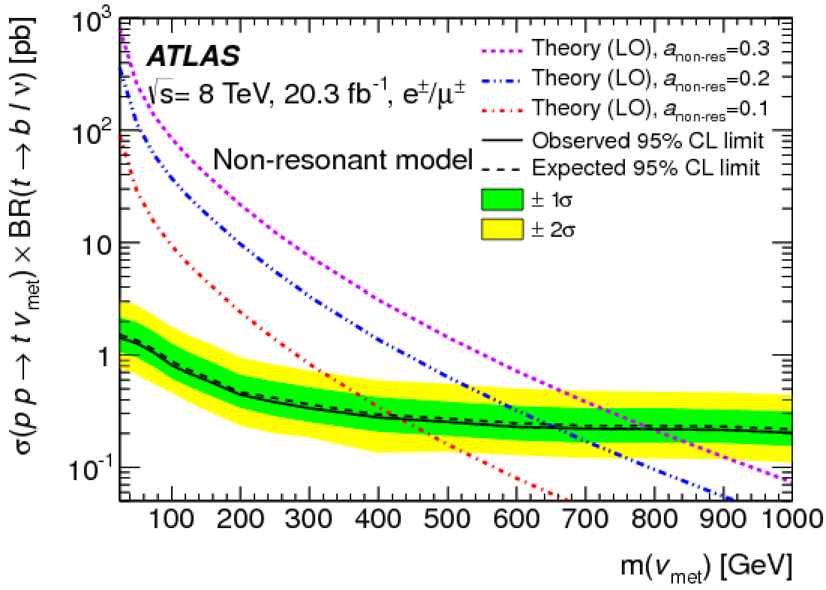

FIGURE 6.1: Observed and expected limits on the cross section times branching ratio for the non-resonant model, as a function of the mass of V (v_{met}). The mass of the invisible spin-1/2 fermion is assumed to be $m(\chi)$=1 GeV [91]. Notice that $a_{non-res}$ is treated as a in this work.

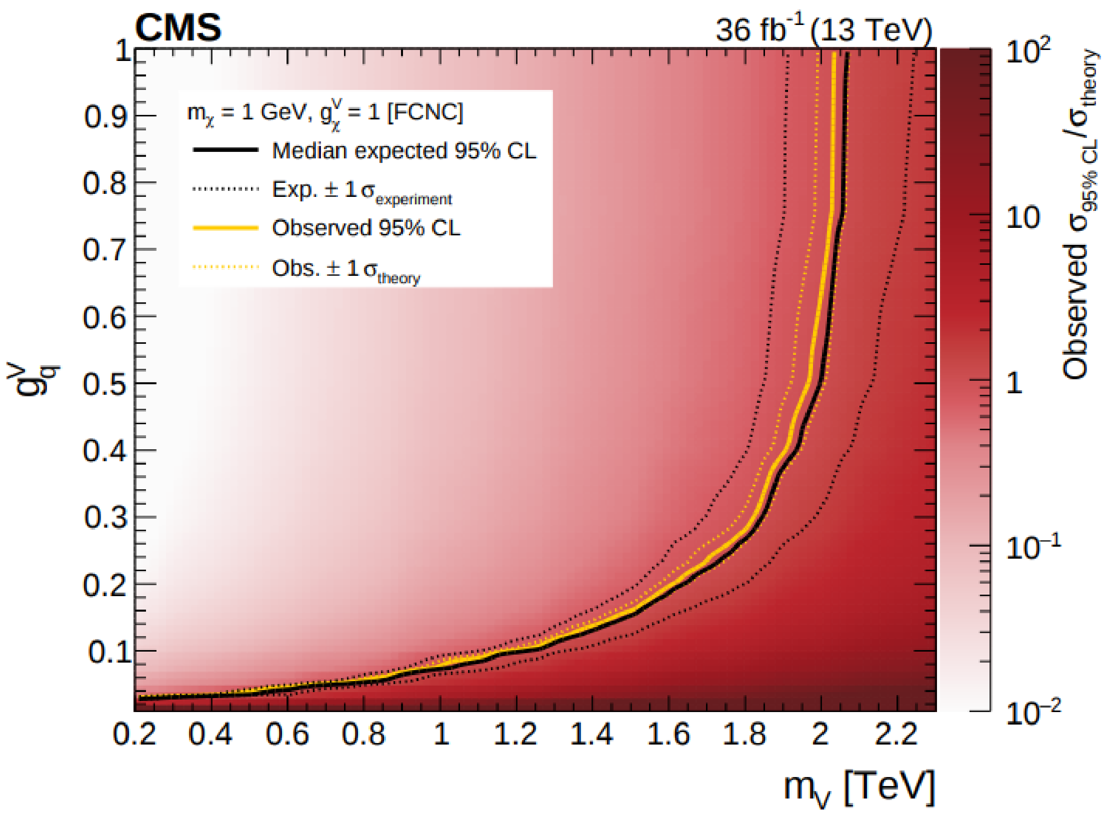

FIGURE 6.2: Results for the non-resonant interpretation presented in the two-dimensional plane spanned by the mediator mass, $m(V)$, and the coupling between the mediator and quarks, g_q^V [94]. The mediator is assumed to have purely vector couplings. The observed exclusion range (gold solid line) is shown. The gold dashed lines show the cases in which the predicted cross section is shifted by the assigned theoretical uncertainty. The expected exclusion range is indicated by a black solid line, demonstrating the search sensitivity of the analysis. The experimental uncertainties are shown in black dashed lines. Notice that g_q^V and g_χ^V are treated as a and g_χ respectively in this work.

and a limit is given for each one. Finally, the most optimal cut region is discussed and compared with the limit obtained with the cut-based selection. As mentioned in Section 4.1.1, the parameter values considered in this analysis are $a = 0.5$, $g_\chi = 1.0$ and the mass of the final state DM Dirac fermion $m_\chi = 1$ GeV.

This calculation is based on the signal strength limit for different masses of the invisible spin-1 state, v_{met}, from 1 to 5 TeV. In order to calculate these limits, the package `TRexFitter` is used [95]. It provides a framework to perform profile likelihood fits on multiple regions with multiple bins, using RooStats. Using the histograms and a configuration file as inputs, it is possible to produce the desired fits, limits, prefit and postfit MC distributions and tables.

The expected signal strength (the ratio of the expected cross section to the SM prediction) limit is calculated for each mass point and a fit is performed. By comparing it with the theoretical curve, a limit on the invisible DM particle mass can be estimated at 95% CL. Figures 6.3, 6.4 and 6.5 show these exclusion limits for preselection, training and SR respectively (where no cut on $oBDT$ is applied). The corresponding exclusion mass limit are 1650, 2020 and 2090 GeV.

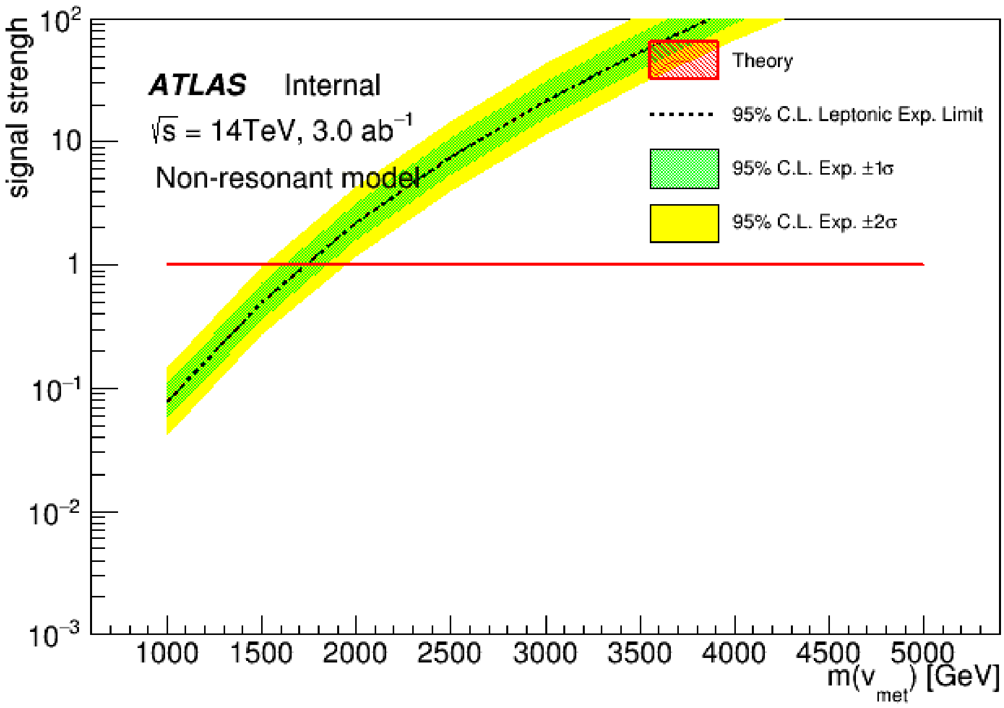

FIGURE 6.3: Expected limits on the signal strength for the non-resonant model, as a function of the mass of (v_{met}), in the signal preselection region. No cut on $oBDT$ is applied.

To optimise the effects of the BDT, different cuts on $oBDT$ are applied, on top of the cuts corresponding to each region, from 0 to +1 in steps of 0.15. As before, the exclusion mass limits are calculated for each new region (which is supposed to be richer in signal events). A summary of these results is shown in Figure 6.6. As it can be observed, the highest limit is achieved in the SR when adding the BDT cut at $oBDT$>0.9.

As it can be checked in Figure 6.7, the value corresponding to this exclusion mass limit at 95% CL is $\sim$ 3.3 TeV. Notice that for masses above 3000 GeV, the 2σ uncertainty band can not be properly estimated due to MC statistical uncertainties. Table 6.1 contains the event yields for the electron and muon channel respectively.

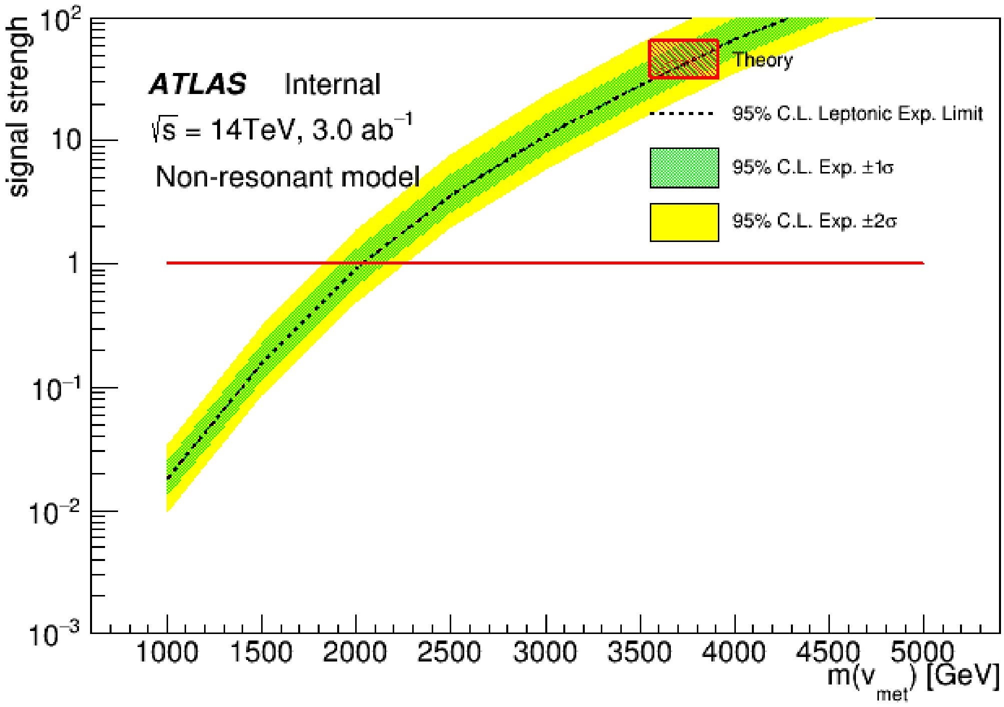

FIGURE 6.4: Expected limits on the signal strength for the non-resonant model, as a function of the mass of (v_{met}), in the training region. No cut on $oBDT$ is applied.

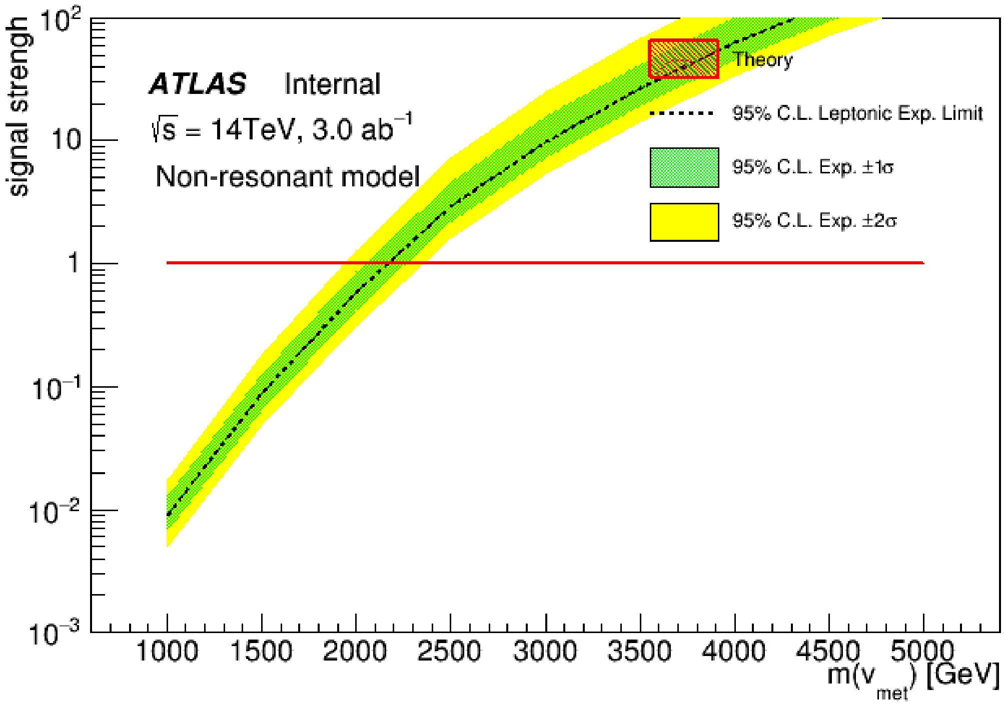

FIGURE 6.5: Expected limits on the signal strength for the non-resonant model, as a function of the mass of (v_{met}), in the SR. No cut on $oBDT$ is applied.

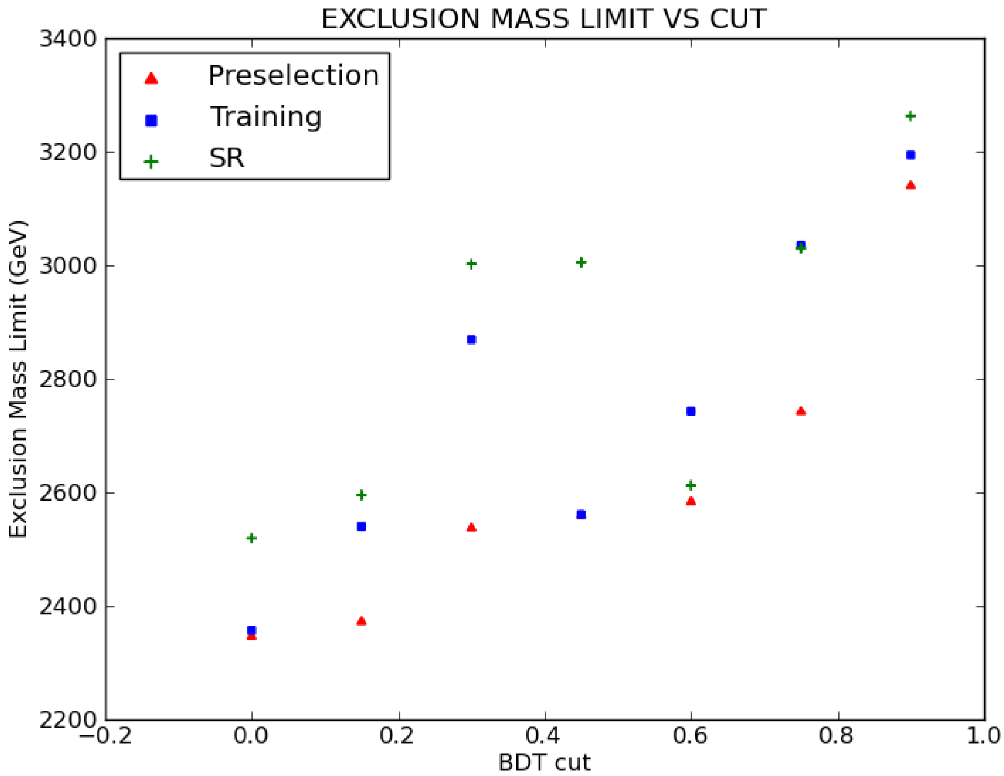

FIGURE 6.6: Mass exclusion limits for different BDT cuts in the three main regions studied: preselection, training and SR.

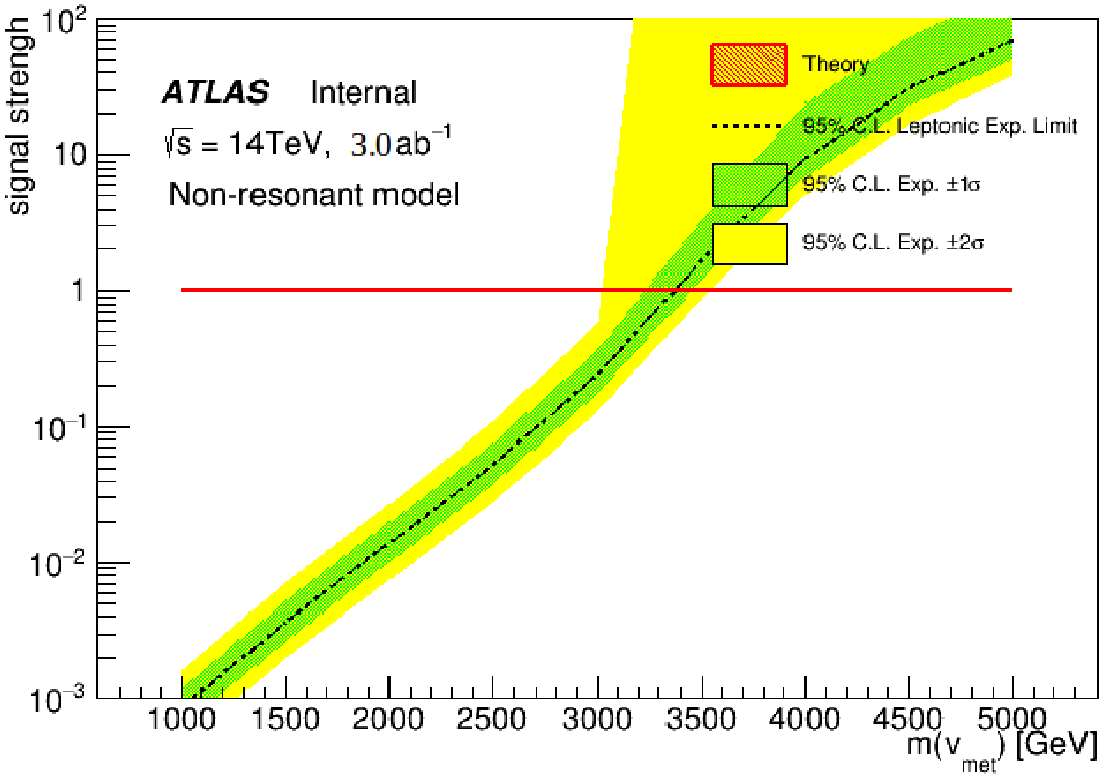

FIGURE 6.7: Expected limits on the signal strength for the non-resonant model, as a function of the mass of (v_{met}), in the SR region with $oBDT$<0.9.

Sample	Electron channel	Muon channel
m_V = 1.0 TeV	28127.53 ± 198.44	29285.66 ± 202.48
m_V = 1.5 TeV	6341.28 ± 38.85	6666.29 ± 39.83
m_V = 2.0 TeV	1737.14 ± 10.01	1803.74 ± 10.20
m_V = 2.5 TeV	530.28 ± 3.03	565.17 ± 3.13
m_V = 3.0 TeV	183.57 ± 1.06	195.00 ± 1.10
m_V = 3.5 TeV	73.00 ± 0.43	76.49 ± 0.44
m_V = 4.0 TeV	30.85 ± 0.19	32.63 ± 0.20
m_V = 4.5 TeV	14.70 ± 0.10	15.41 ± 0.10
m_V = 5.0 TeV	7.88 ± 0.05	8.19 ± 0.05
SgTop	0.00 ± 0.00	0.00± 0.00
Top	309.23 ± 126.24	309.34± 126.29
W+jets	230.54 ± 114.92	394.98 ± 157.08
Z+jets, Diboson	0.00 ± 0.00	0.99 ± 0.99

TABLE 6.1: Event yields for the SR, with $oBDT$>0.90. Electron and muon channel are considered separately.

Chapter 7

Conclusions

7.1 Conclusions

The expected sensitivity of a search for events with one top quark and large missing transverse momentum at the final state is estimated in pp collisions at $\sqrt{s} = 14$ TeV with the ATLAS experiment at the HL-LHC. A non-resonant production of an invisible exotic particle in association with a right-handed top quark is considered, where the W boson from the top quark is required to decay into an electron or a muon and a neutrino. An estimated upper limit of 3.3 TeV based on a BDT discriminant analysis, at 95% CL, assuming an integrated luminosity of 3.0 ab^{-1}, is set on the non-resonant monotop cross-section.

For the parameter values considered in this work, the mediator mass was excluded up to 2.0 TeV by CMS Collaboration using 36 fb^{-1} at $\sqrt{s}$ = 13 TeV (see Figure 6.2), so an increase of $\sim$ 1.3 TeV is expected. Therefore, it is checked that higher integrated luminosity and center-of-mass energy lead to the possibility of restricting even more the mass range of the invisible neutral boson.

Finally, it is also concluded that a new and improved optimised selection of monotop events has been achieved via the use of a BDT. The parameters of the BDT were explored to obtain an optimum performance, as described in Section 5.4.3, and a single discriminant output, $oBDT$, was correctly manipulated to apply a single cut to the sample in order to obtain even better exclusion mass limits. As it can be seen in Section 6.2, the limit is improved from 2.1 to 3.3 TeV in the signal region when using the MVA. Furthermore, not only does the BDT based method offer the advantage of an improved optimisation, but also the use of the single cut in the discriminant $oBDT$ allows for an easier and simpler procedure as opposed to applying a series of separate cuts in multiple variables without taking into account all their correlations.

7.2 Future Work

A MVA offers several possibilities in order to optimise event selections in particle physics. Among them, there is one which could be firstly implemented and hopefully improve the exclusion mass limit presented in this work. The idea would be to train the BDT, not only with the monotop signal for m_V=3000 Gev and $t\bar{t}$ process as background, but adding also the whole set of processes (signal and background ones) with their corresponding event weights. Like this, it is expected to potentially increase the background rejection, maintaining the high signal efficiency.

Appendix A

Evaluation of the available MVA methods

Among the several available methods it could be chosen, BDTG (BDT trained with the Gradient algorithm) is considered despite its results were compatible with the ones obtained through other MVA techniques such as BDT (BDT trained with the AdaBoost algorithm) or Artificial Neural Networks (MLP and MLPBNN). Figure A.1 shows the ROC curve (signal efficiency vs. background rejection) for each discussed classifier together. Table A.1 gives the performance evaluation values.

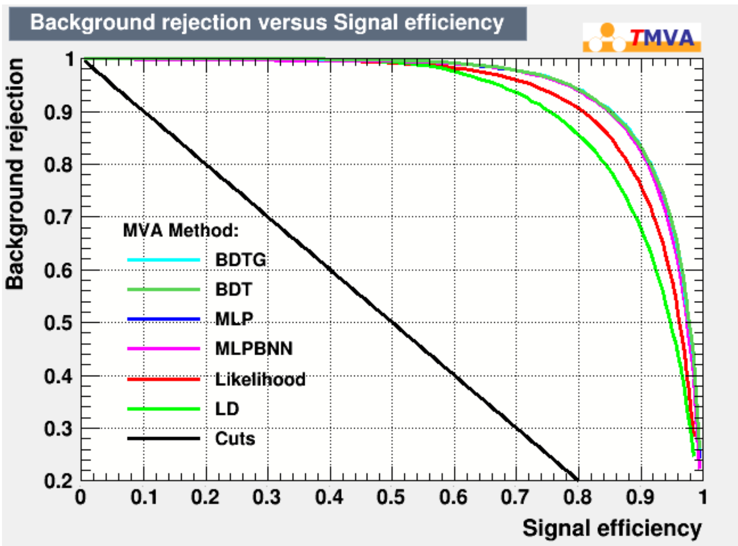

FIGURE A.1: ROC curve obtained for the different MVA method available in the TMVA package. Legend ranks the methods from highest to lowest ROC integral value.

MVA Method	Roc-integral	Separation	Significance
BDTG	0.947	0.647	1.898
BDT	0.947	0.641	1.654
MLP	0.944	0.637	1.865
MLPBNN	0.943	0.635	1.844
Likelihood	0.925	0.580	1.237
LD	0.907	0.513	1.190
Cuts	0.500	–	–

TABLE A.1: Values corresponding to the ROC curve integral, Separation and Significane for each MVA method considered.

Appendix B

Significance and S/B for different BDT cuts

Some orientative plots showing the signal to background ratio (S/B) vs. the statistical significance ($\frac{S}{\sqrt{S+B}}$) for each BDT cut are presented in Figures B.1, B.2 and B.3. The granularity of the BDT cut is set to 0.02 and the plots are produced for each region considered in this analysis. Top-right corner points correspond to the highest BDT cut values.

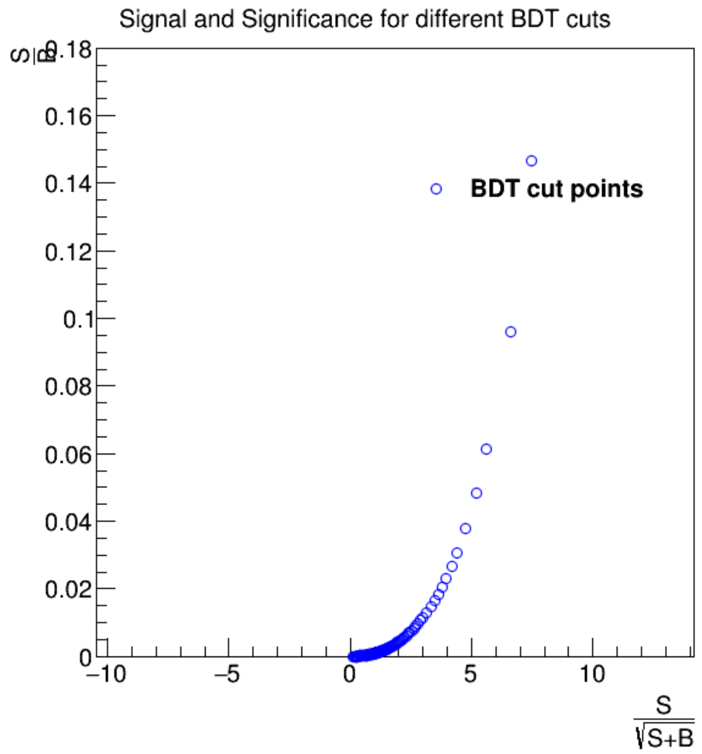

FIGURE B.1: S/B vs. significance for different cuts in the signal preselection region.

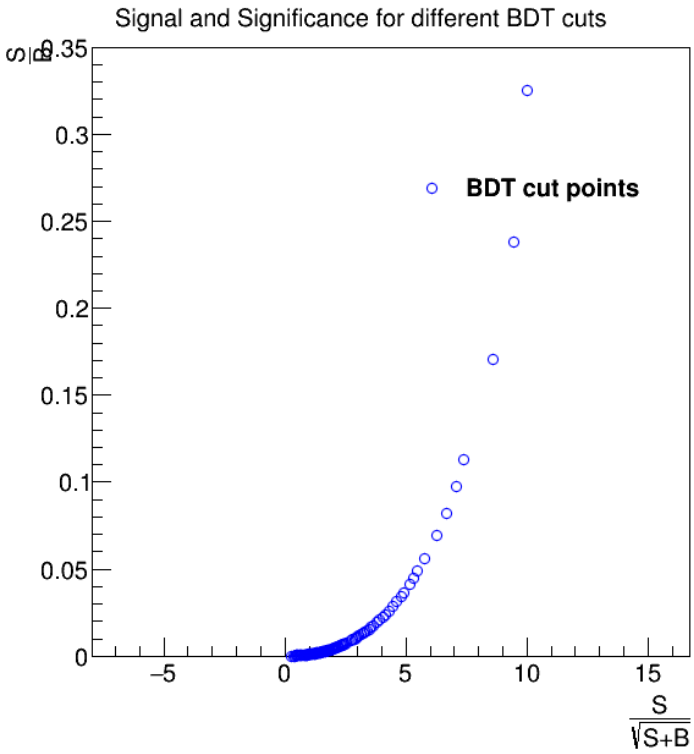

FIGURE B.2: S/B vs. significance for different cuts in the training region

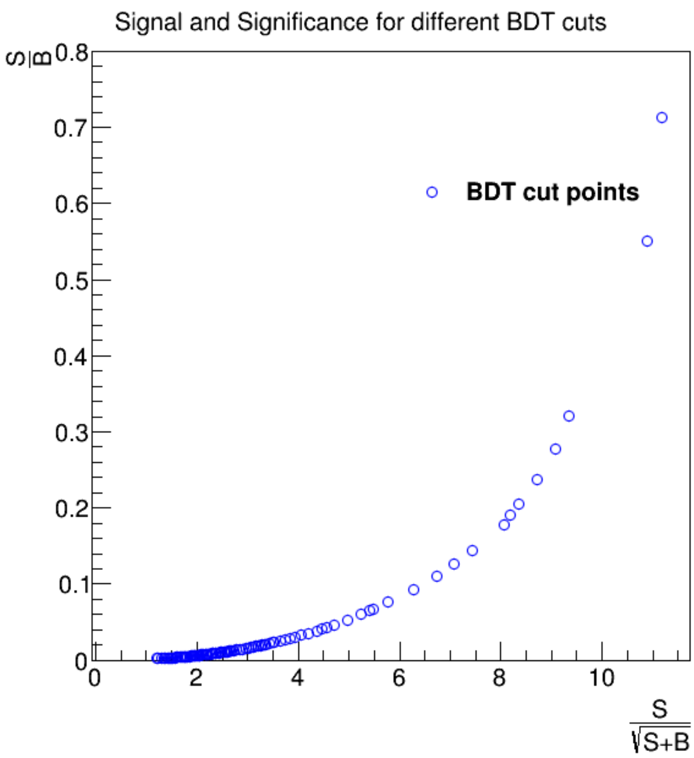

FIGURE B.3: S/B vs. significance for different cuts in the signal region (SR)

Acknowledgements

I would like to thank my supervisors, José Enrique and Carlos, for the guidance and advice they have provided throughout my time as their student. I would also like to thank Daniele (grazie mille!) and Florencia (muchas gracias!) who helped me in my supervisors' absence and whenever I had a difficulty. I would also like to thank the rest of the ATLAS group members for the nice reception, in particular to Laura and Susana for the suggestions they made in reference to `TMVA` and `TRexFitter` operation details. I must express my gratitude to my mother, father and brother for their continued support and encouragement. Gràcies per cuidar-me tan bé i tindre tanta paciència amb mi. Completing this work would have been all the more difficult were it not for the support and friendship provided by Kevin, Pablo and Marcos. Sigué una sort trobar-me amb els millors companys de despatx que haguera pogut demanar.

Bibliography

[1] S. Chatrchyan et al. "Observation of a new boson at a mass of 125 GeV with the CMS experiment at the LHC". In: *Physics Letters B* 716.1 (2012), pp. 30–61. ISSN: 0370-2693. DOI: https://doi.org/10.1016/j.physletb.2012.08.021. URL: http://www.sciencedirect.com/science/article/pii/S0370269312008581.

[2] G. Aad et al. "Observation of a new particle in the search for the Standard Model Higgs boson with the ATLAS detector at the LHC". In: *Physics Letters B* 716.1 (2012), pp. 1–29. ISSN: 0370-2693. DOI: https://doi.org/10.1016/j.physletb.2012.08.020. URL: http://www.sciencedirect.com/science/article/pii/S037026931200857X.

[3] Peter W. Higgs. "Broken Symmetries and the Masses of Gauge Bosons". In: *Phys. Rev. Lett.* 13 (16 Oct. 1964), pp. 508–509. DOI: 10.1103/PhysRevLett.13.508. URL: https://link.aps.org/doi/10.1103/PhysRevLett.13.508.

[4] F. Englert and R. Brout. "Broken Symmetry and the Mass of Gauge Vector Mesons". In: *Phys. Rev. Lett.* 13 (9 Aug. 1964), pp. 321–323. DOI: 10.1103/PhysRevLett.13.321. URL: https://link.aps.org/doi/10.1103/PhysRevLett.13.321.

[5] Edvige Corbelli and Paolo Salucci. "The extended rotation curve and the dark matter halo of M33". In: *Monthly Notices of the Royal Astronomical Society* 311.2 (2000), pp. 441–447. DOI: 10.1046/j.1365-8711.2000.03075.x. eprint: /oup/backfile/content_public/journal/mnras/311/2/10.1046/j.1365-8711.2000.03075.x/2/311-2-441.pdf. URL: http://dx.doi.org/10.1046/j.1365-8711.2000.03075.x.

[6] Wikipedia contributors. *Galaxy rotation curve — Wikipedia, The Free Encyclopedia*. [Online; accessed 14-August-2018]. 2018. URL: https://en.wikipedia.org/w/index.php?title=Galaxy_rotation_curve&oldid=851034848.

[7] Laura Baudis. "The Search for Dark Matter". In: *European Review* 26.1 (2018), pp. 70–81. DOI: 10.1017/S1062798717000783.

[8] Edgar Bugaev and Peter Klimai. "Large curvature perturbations near horizon crossing in single-field inflation models". In: *Phys. Rev. D* 78 (6 Sept. 2008), p. 063515. DOI: 10.1103/PhysRevD.78.063515. URL: https://link.aps.org/doi/10.1103/PhysRevD.78.063515.

[9] Bernard Carr et al. "Primordial black hole constraints for extended mass functions". In: *Phys. Rev. D* 96 (2 July 2017), p. 023514. DOI: 10.1103/PhysRevD.96.023514. URL: https://link.aps.org/doi/10.1103/PhysRevD.96.023514.

[10] Kevork Abazajian, George M. Fuller, and Mitesh Patel. "Sterile neutrino hot, warm, and cold dark matter". In: *Phys. Rev. D* 64 (2 May 2001), p. 023501. DOI: 10.1103/PhysRevD.64.023501. URL: https://link.aps.org/doi/10.1103/PhysRevD.64.023501.

[11] H. Goldberg. "Constraint on the Photino Mass from Cosmology". In: *Phys. Rev. Lett.* 50 (1983). [,219(1983)], p. 1419. DOI: 10.1103/PhysRevLett.103.099905,10.1103/PhysRevLett.50.1419.

[12] John Ellis et al. "Supersymmetric relics from the big bang". In: *Nuclear Physics B* 238.2 (1984), pp. 453–476. ISSN: 0550-3213. DOI: https://doi.org/10.1016/0550-3213(84)90461-9. URL: http://www.sciencedirect.com/science/article/pii/0550321384904619.

[13] Hsin-Chia Cheng and Ian Low. "TeV symmetry and the little hierarchy problem". In: *Journal of High Energy Physics* 2003.09 (2003), p. 051. URL: http://stacks.iop.org/1126-6708/2003/i=09/a=051.

[14] Andreas Birkedal et al. "Little Higgs dark matter". In: *Phys. Rev. D* 74 (3 Aug. 2006), p. 035002. DOI: 10.1103/PhysRevD.74.035002. URL: https://link.aps.org/doi/10.1103/PhysRevD.74.035002.

[15] Michael Dine, Willy Fischler, and Mark Srednicki. "Supersymmetric Technicolor". In: *Nucl. Phys.* B189 (1981), pp. 575–593. DOI: 10.1016/0550-3213(81)90582-4.

[16] CSABA CSÁKI. "THE MINIMAL SUPERSYMMETRIC STANDARD MODEL". In: *Modern Physics Letters A* 11.08 (1996), pp. 599–613. DOI: 10.1142/S021773239600062X. eprint: https://doi.org/10.1142/S021773239600062X. URL: https://doi.org/10.1142/S021773239600062X.

[17] Michele Gallinaro. "Top quark physics: A tool for discoveries". In: *Journal of Physics: Conference Series* 447.1 (2013), p. 012012. URL: http://stacks.iop.org/1742-6596/447/i=1/a=012012.

[18] ATLAS Collaboration. "Search for dark matter at $\sqrt{s} = 13$ TeV in final states containing an energetic photon and large missing transverse momentum with the ATLAS detector". In: *Eur. Phys. J.* C77.6 (2017), p. 393. DOI: 10.1140/epjc/s10052-017-4965-8. arXiv: 1704.03848 [hep-ex].

[19] CMS Collaboration. "Search for new physics in the monophoton final state in proton-proton collisions at $\sqrt{s} = 13$ TeV". In: *JHEP* 10 (2017), p. 073. DOI: 10.1007/JHEP10(2017)073. arXiv: 1706.03794 [hep-ex].

[20] ATLAS Collaboration. "Search for dark matter and other new phenomena in events with an energetic jet and large missing transverse momentum using the ATLAS detector". In: *JHEP* 01 (2018), p. 126. DOI: 10.1007/JHEP01(2018)126. arXiv: 1711.03301 [hep-ex].

[21] CMS Collaboration. "Search for dark matter produced with an energetic jet or a hadronically decaying W or Z boson at $\sqrt{s} = 13$ TeV". In: *JHEP* 07 (2017), p. 014. DOI: 10.1007/JHEP07(2017)014. arXiv: 1703.01651 [hep-ex].

[22] ATLAS Collaboration. "Search for dark matter produced in association with bottom or top quarks in $\sqrt{s} = 13$ TeV pp collisions with the ATLAS detector". In: *Eur. Phys. J.* C78.1 (2018), p. 18. DOI: 10.1140/epjc/s10052-017-5486-1. arXiv: 1710.11412 [hep-ex].

[23] ATLAS Collaboration. "Search for top-squark pair production in final states with one lepton, jets, and missing transverse momentum using 36 fb^{-1} of $\sqrt{s} = 13$ TeV pp collision data with the ATLAS detector". In: (2017). arXiv: 1711.11520 [hep-ex].

[24] ATLAS Collaboration. "Search for Dark Matter Produced in Association with a Higgs Boson Decaying to $b\bar{b}$ using 36 fb^{-1} of pp collisions at $\sqrt{s} = 13$ TeV with the ATLAS Detector". In: *Phys. Rev. Lett.* 119.18 (2017), p. 181804. DOI: 10.1103/PhysRevLett.119.181804. arXiv: 1707.01302 [hep-ex].

[25] ATLAS Collaboration. "Search for dark matter in association with a Higgs boson decaying to two photons at $\sqrt{s} = 13$ TeV with the ATLAS detector". In: *Phys. Rev.* D96.11 (2017), p. 112004. DOI: 10.1103/PhysRevD.96.112004. arXiv: 1706.03948 [hep-ex].

[26] CMS Collaboration. "Search for associated production of dark matter with a Higgs boson decaying to $\mathrm{b}\bar{\mathrm{b}}$ or $\gamma\gamma$ at $\sqrt{s} = 13$ TeV". In: *JHEP* 10 (2017), p. 180. DOI: 10.1007/JHEP10(2017)180. arXiv: 1703.05236 [hep-ex].

[27] ATLAS Collaboration. "Search for dark matter produced in association with a hadronically decaying vector boson in pp collisions at $\sqrt{s} = 13$ TeV with the ATLAS detector". In: *Phys. Lett.* B763 (2016), pp. 251–268. DOI: 10.1016/j.physletb.2016.10.042. arXiv: 1608.02372 [hep-ex].

[28] ATLAS Collaboration. "Search for an invisibly decaying Higgs boson or dark matter candidates produced in association with a Z boson in pp collisions at $\sqrt{s} = 13$ TeV with the ATLAS detector". In: *Phys. Lett.* B776 (2018), pp. 318–337. DOI: 10.1016/j.physletb.2017.11.049. arXiv: 1708.09624 [hep-ex].

[29] M. Aaboud et al. "Measurement of the production cross-section of a single top quark in association with a Z boson in proton–proton collisions at 13 TeV with the ATLAS detector". In: *Physics Letters B* 780 (2018), pp. 557–577. ISSN: 0370-2693. DOI: https://doi.org/10.1016/j.physletb.2018.03.023. URL: http://www.sciencedirect.com/science/article/pii/S0370269318302120.

[30] Edmond L. Berger, B. W. Harris, and Z. Sullivan. "Single-Top-Squark Production via *R*-Parity-Violating Supersymmetric Couplings in Hadron Collisions". In: *Phys. Rev. Lett.* 83 (22 Nov. 1999), pp. 4472–4475. DOI: 10.1103/PhysRevLett.83.4472. URL: https://link.aps.org/doi/10.1103/PhysRevLett.83.4472.

[31] Edmond L. Berger, B. W. Harris, and Z. Sullivan. "Direct probes of R-parity violating supersymmetric couplings via single top squark production". In: *Phys. Rev.* D63 (2001), p. 115001. DOI: 10.1103/PhysRevD.63.115001. arXiv: hep-ph/0012184 [hep-ph].

[32] Nishita Desai and Biswarup Mukhopadhyaya. "R-parity violating resonant stop production at the Large Hadron Collider". In: *Journal of High Energy Physics* 2010.10 (Oct. 2010),

p. 60. ISSN: 1029-8479. DOI: 10.1007/JHEP10(2010)060. URL: https://doi.org/10.1007/JHEP10(2010)060.

[33] Benjamin Fuks. "Beyond the Minimal Supersymmetric Standard Model: from theory to phenomenology". In: *International Journal of Modern Physics A* 27.07 (2012), p. 1230007. DOI: 10.1142/S0217751X12300074. eprint: https://doi.org/10.1142/S0217751X12300074. URL: https://doi.org/10.1142/S0217751X12300074.

[34] Hooman Davoudiasl et al. "Baryon Destruction by Asymmetric Dark Matter". In: *Phys. Rev.* D84 (2011), p. 096008. DOI: 10.1103/PhysRevD.84.096008. arXiv: 1106.4320 [hep-ph].

[35] Jernej F. Kamenik and Jure Zupan. "Discovering Dark Matter Through Flavor Violation at the LHC". In: *Phys. Rev.* D84 (2011), p. 111502. DOI: 10.1103/PhysRevD.84.111502. arXiv: 1107.0623 [hep-ph].

[36] Ezequiel Alvarez et al. "Leptonic Monotops at LHC". In: *Phys. Rev.* D89.1 (2014), p. 014016. DOI: 10.1103/PhysRevD.89.014016. arXiv: 1310.7600 [hep-ph].

[37] Hooman Davoudiasl et al. "Unified Origin for Baryonic Visible Matter and Antibaryonic Dark Matter". In: *Phys. Rev. Lett.* 105 (21 Nov. 2010), p. 211304. DOI: 10.1103/PhysRevLett.105.211304. URL: https://link.aps.org/doi/10.1103/PhysRevLett.105.211304.

[38] Jean-Laurent Agram et al. "Monotop phenomenology at the Large Hadron Collider". In: *Phys. Rev.* D89.1 (2014), p. 014028. DOI: 10.1103/PhysRevD.89.014028. arXiv: 1311.6478 [hep-ph].

[39] Zhe Dong et al. "Baryon number violation at the LHC: the top option". In: *Phys. Rev.* D85 (2012), p. 016006. DOI: 10.1103/PhysRevD.85.016006, 10.1103/PhysRevD.85.039907. arXiv: 1107.3805 [hep-ph].

[40] F. del Aguila, J. A. Aguilar-Saavedra, and L. Ametller. "Z t and gamma t production via top flavor changing neutral couplings at the Fermilab Tevatron". In: *Phys. Lett.* B462 (1999), pp. 310–318. DOI: 10.1016/S0370-2693(99)00929-6. arXiv: hep-ph/9906462 [hep-ph].

[41] Idir Boucheneb et al. "Revisiting monotop production at the LHC". In: *Journal of High Energy Physics* 2015.1 (Jan. 2015), p. 17. ISSN: 1029-8479. DOI: 10.1007/JHEP01(2015)017. URL: https://doi.org/10.1007/JHEP01(2015)017.

[42] CERN. *About Cern*. URL: https://home.cern/about.

[43] CERN. *The accelerator complex*. 2008. URL: http://public-archive.web.cern.ch/public-archive/en/research/AccelComplex-en.html.

[44] CERN. *The Large Hadron Collider*. URL: https://home.cern/topics/large-hadron-collider.

[45] CERN. *How an Accelerator Works*. 2018. URL: https://home.cern/about/how-accelerator-works.

[46] CERN. *Radiofrequency Cavities*. 2018. URL: https://home.cern/about/engineering/radiofrequency-cavities.

[47] The ATLAS Collaboration et all. "The ATLAS Experiment at the CERN Large Hadron Collider". In: *Journal of Instrumentation* 3.08 (2008), S08003. URL: http://stacks.iop.org/1748-0221/3/i=08/a=S08003.

[48] Prof. C. Anastasiou et all. "Particle Physics Phenomenology 1 – HS 2010". In: ed. by A. Reimer. 2010. Chap. Accelerators and collider experiments. URL: http://edu.itp.phys.ethz.ch/hs10/ppp1/PPP1_4.pdf.

[49] Werner Herr and B Muratori. "Concept of luminosity". In: (2006). URL: http://cds.cern.ch/record/941318.

[50] J G Panduro Vazquez. *The ATLAS Data Acquisition System: from Run 1 to Run 2*. Tech. rep. ATL-DAQ-PROC-2014-035. Geneva: CERN, Oct. 2014. URL: https://cds.cern.ch/record/1954156.

[51] A. Hoecker. "Physics at the LHC Run-2 and Beyond". In: *ArXiv e-prints* (Nov. 2016). arXiv: 1611.07864 [hep-ex].

[52] C. Patrignani and Particle Data Group. "Review of Particle Physics". In: *Chinese Physics C* 40.10 (2016), p. 100001. URL: http://stacks.iop.org/1674-1137/40/i=10/a=100001.

[53] CERN. *The Inverse Femtobarn*. URL: http://writing-guidelines.web.cern.ch/entries/inverse-femtobarn.

[54] Roderik Bruce et al. "LHC Run 2: Results and challenges". In: CERN-ACC-2016-0103 (July 2016), MOAM5P50. 7 p. URL: https://cds.cern.ch/record/2201447.

[55] ATLAS. *ATLAS Experiment - Public Results*. 2018. URL: https://twiki.cern.ch/twiki/bin/view/AtlasPublic/LuminosityPublicResultsRun2.

[56] ATLAS. *ATLAS Experiment - Public Results*. URL: https://twiki.cern.ch/twiki/bin/view/AtlasPublic/LuminosityPublicResultsRun2.
[57] ATLAS. *Detector and Technology*. URL: https://atlas.cern/discover/detector.
[58] G. Apollinari et al. "Chapter 1: High Luminosity Large Hadron Collider HL-LHC. High Luminosity Large Hadron Collider HL-LHC". In: *CERN Yellow Report* arXiv:1705.08830. 5 (May 2017). 21 pages, chapter in High-Luminosity Large Hadron Collider (HL-LHC) : Preliminary Design Report, 1–19. 21 p. URL: https://cds.cern.ch/record/2120673.
[59] ATLAS Collaboration. *Technical Design Report for the ATLAS Inner Tracker Pixel Detector*. Tech. rep. CERN-LHCC-2017-021. ATLAS-TDR-030. Geneva: CERN, 2017. URL: https://cds.cern.ch/record/2285585.
[60] ATLAS Collaboration. *Technical Design Report for the ATLAS Inner Tracker Strip Detector*. Tech. rep. CERN-LHCC-2017-005. ATLAS-TDR-025. Geneva: CERN, 2017. URL: https://cds.cern.ch/record/2257755.
[61] ATLAS Collaboration. *Technical Design Report for the Phase-II Upgrade of the ATLAS LAr Calorimeter*. Tech. rep. CERN-LHCC-2017-018. ATLAS-TDR-027. Geneva: CERN, 2017. URL: https://cds.cern.ch/record/2285582.
[62] ATLAS Collaboration. *Technical Design Report for the Phase-II Upgrade of the ATLAS Tile Calorimeter*. Tech. rep. CERN-LHCC-2017-019. ATLAS-TDR-028. Geneva: CERN, 2017. URL: https://cds.cern.ch/record/2285583.
[63] ATLAS Collaboration. *Technical Design Report for the Phase-II Upgrade of the ATLAS Muon Spectrometer*. Tech. rep. CERN-LHCC-2017-017. ATLAS-TDR-026. Geneva: CERN, 2017. URL: https://cds.cern.ch/record/2285580.
[64] ATLAS Collaboration. *Technical Design Report for the Phase-II Upgrade of the ATLAS TDAQ System*. Tech. rep. CERN-LHCC-2017-020. ATLAS-TDR-029. Geneva: CERN, 2017. URL: https://cds.cern.ch/record/2285584.
[65] ATLAS Collaboration. "The ATLAS Simulation Infrastructure". In: *Eur. Phys. J. C* 70 (2010), p. 823. DOI: 10.1140/epjc/s10052-010-1429-9. arXiv: 1005.4568 [physics.ins-det].
[66] J. Alwall et al. "The automated computation of tree-level and next-to-leading order differential cross sections, and their matching to parton shower simulations". In: *JHEP* 07 (2014), p. 079. DOI: 10.1007/JHEP07(2014)079. arXiv: 1405.0301 [hep-ph].
[67] Richard D. Ball et al. "Parton distributions for the LHC Run II". In: *JHEP* 04 (2015), p. 040. DOI: 10.1007/JHEP04(2015)040. arXiv: 1410.8849 [hep-ph].
[68] Torbjorn Sjostrand, Stephen Mrenna, and Peter Z. Skands. "A Brief Introduction to PYTHIA 8.1". In: *Comput. Phys. Commun.* 178 (2008), pp. 852–867. DOI: 10.1016/j.cpc.2008.01.036. arXiv: 0710.3820 [hep-ph].
[69] ATLAS Collaboration. *ATLAS Pythia 8 tunes to 7 TeV data*. ATL-PHYS-PUB-2014-021. 2014. URL: https://cds.cern.ch/record/1966419.
[70] Richard D. Ball et al. "Parton distributions with LHC data". In: *Nucl. Phys.* B867 (2013), pp. 244–289. DOI: 10.1016/j.nuclphysb.2012.10.003. arXiv: 1207.1303 [hep-ph].
[71] D. J. Lange. "The EvtGen particle decay simulation package". In: *Nucl. Instrum. Meth.* A462 (2001), pp. 152–155. DOI: 10.1016/S0168-9002(01)00089-4.
[72] Muhammad Alhroob et al. *Search for invisible particles produced in association with single-top-quarks in proton–proton collisions at $\sqrt{s}$ = 13 TeV with the ATLAS detector*. Tech. rep. ATL-COM-PHYS-2018-038. Geneva: CERN, 2018. URL: https://cds.cern.ch/record/2301180.
[73] Simone Alioli et al. "A general framework for implementing NLO calculations in shower Monte Carlo programs: the POWHEG BOX". In: *JHEP* 06 (2010), p. 043. DOI: 10.1007/JHEP06(2010)043. arXiv: 1002.2581 [hep-ph].
[74] Hung-Liang Lai et al. "New parton distributions for collider physics". In: *Phys. Rev.* D82 (2010), p. 074024. DOI: 10.1103/PhysRevD.82.074024. arXiv: 1007.2241 [hep-ph].
[75] Peter Zeiler Skands. "Tuning Monte Carlo Generators: The Perugia Tunes". In: *Phys. Rev.* D82 (2010), p. 074018. DOI: 10.1103/PhysRevD.82.074018. arXiv: 1005.3457 [hep-ph].
[76] ATLAS Collaboration. *ATLAS Phase-II Upgrade Scoping Document*. Tech. rep. CERN-LHCC-2015-020. LHCC-G-166. Geneva: CERN, 2015. URL: https://cds.cern.ch/record/2055248.
[77] ATLAS Collaboration. "UpgradePerformanceFunctions twiki". In: (2018). URL: https://twiki.cern.ch/twiki/bin/view/AtlasProtected/UpgradePerformanceFunctions.
[78] ATLAS Collaboration. *Expected pile-up values at the HL-LHC*. ATL-UPGRADE-PUB-2013-014. 2013. URL: https://cds.cern.ch/record/1604492.

[79] ATLAS Collaboration. *Expected performance for an upgraded ATLAS detector at High-Luminosity LHC*. ATL-PHYS-PUB-2016-026. 2016. URL: https://cds.cern.ch/record/2223839.
[80] ATLAS Collaboration. "ATLAS AnalysisTop framework twiki". In: (2018). URL: https://twiki.cern.ch/twiki/bin/view/AtlasProtected/AnalysisTop21#AnalysisTop_21_2_35_27_June_18_S.
[81] Andy Buckley et al. "Rivet user manual". In: *Comput. Phys. Commun.* 184 (2013), pp. 2803–2819. DOI: 10.1016/j.cpc.2013.05.021. arXiv: 1003.0694 [hep-ph].
[82] ATLAS Collaboration. *Performance assumptions based on full simulation for an upgraded ATLAS detector at a High-Luminosity LHC*. ATL-PHYS-PUB-2013-009. 2013. URL: https://cds.cern.ch/record/1604420.
[83] Matteo Cacciari, Gavin P. Salam, and Gregory Soyez. "The Anti-k(t) jet clustering algorithm". In: *JHEP* 04 (2008), p. 063. DOI: 10.1088/1126-6708/2008/04/063. arXiv: 0802.1189 [hep-ph].
[84] Matteo Cacciari, Gavin P. Salam, and Gregory Soyez. "FastJet User Manual". In: *Eur. Phys. J.* C72 (2012), p. 1896. DOI: 10.1140/epjc/s10052-012-1896-2. arXiv: 1111.6097 [hep-ph].
[85] ATLAS Collaboration. *Technical Design Report for the ATLAS Inner Tracker Strip Detector*. CERN-LHCC-2017-005, ATLAS-TDR-025. 2017. URL: http://cds.cern.ch/record/2257755.
[86] ATLAS Collaboration. "Performance of b-jet identification in the ATLAS experiment". In: *JINST* 11 (2016), P04008. DOI: 10.1088/1748-0221/11/04/P04008. arXiv: 1512.01094 [hep-ex].
[87] John R. Koza et al. "Automated Design of Both the Topology and Sizing of Analog Electrical Circuits Using Genetic Programming". In: *Artificial Intelligence in Design '96*. Ed. by John S. Gero and Fay Sudweeks. Dordrecht: Springer Netherlands, 1996, pp. 151–170. DOI: 10.1007/978-94-009-0279-4_9. URL: https://doi.org/10.1007/978-94-009-0279-4_9.
[88] Pushpalatha C. Bhat. "Advanced Analysis Methods in Particle Physics". In: *FermiLab Techincal Publications* 10.425 ().
[89] A. Hoecker et al. "TMVA - Toolkit for Multivariate Data Analysis". In: *PoS* (Mar. 2007). eprint: physics/0703039.
[90] David Ciupke. *Study of BDT Training Configurations with an Application to the $Z/H \to \tau\tau \to ee$ Analysis*. University of Göttingen. Germany, 6 September 2012. URL: http://www.desy.de/f/students/2012/reports/david_ciupke.pdf.gz.
[91] "Search for invisible particles produced in association with single-top-quarks in proton-proton collisions at 8 TeV with the ATLAS detector". In: *Eur. Phys. J. C* (2015), 75:79.
[92] T. Aaltonen et al. "Search for a Dark Matter Candidate Produced in Association with a Single Top Quark in $p\overline{p}$ Collisions at $\sqrt{s} = 1.96$ TeV". In: *Phys. Rev. Lett.* 108 (20 May 2012), p. 201802. DOI: 10.1103/PhysRevLett.108.201802. URL: https://link.aps.org/doi/10.1103/PhysRevLett.108.201802.
[93] V. Khachatryan et al. "Search for Monotop Signatures in Proton-Proton Collisions at $\sqrt{s} = 8$ TeV". In: *Phys. Rev. Lett.* 114 (10 Mar. 2015), p. 101801. DOI: 10.1103/PhysRevLett.114.101801. URL: https://link.aps.org/doi/10.1103/PhysRevLett.114.101801.
[94] The CMS collaboration. "Search for dark matter in events with energetic, hadronically decaying top quarks and missing transverse momentum at $\sqrt{s}$=13 TeV". In: *J High Energ. Phys.* (2018), p. 27. DOI: https://doi.org/10.1007/JHEP06(2018)027.
[95] ATLAS Collaboration. *Twiki page for TRexFitter/TthFitter tool (Internal)*. [Online; accessed 28-August-2018]. 2016. URL: https://twiki.cern.ch/twiki/bin/view/AtlasProtected/TtHFitter.